



33 1. INTRODUCTION

34 Massive ice sheets or mountain glaciers respond to various climatic forcing functions that operate on wide
35 scales from local to global. Winter precipitation and summer air temperature are generally considered the most critical
36 factors in controlling glacial mass balance and extent. Understanding the impact of climate on past glacial cycles
37 necessitates a thorough understanding of the timing and amplitude of glacial dynamics. The most recent planet-wide
38 glacial expansion occurred during the Global Last Glacial maximum (gLGM) as a result of changes in major climate
39 forcings, e.g., reduced summer insolation, tropical sea surface temperatures, and atmospheric CO₂. The remnants of
40 paleoglacial deposits of gLGM are the best preserved among all the ice ages. The gLGM has been extensively studied
41 to ascertain the late Pleistocene changes in ice volume, sea-level fluctuations, feedback on climate, etc. The timing of
42 gLGM has been established using both the marine (e.g., Skinner and Shackleton, 2005; Thompson et al., 2003;
43 Shackleton, 2000; Shackleton, 1967) and terrestrial (e.g., Fletcher et al., 2010; Clark et al., 2009; Jouzel et al., 2007;
44 Wang et al., 2001; An et al., 1991) paleoclimatic proxies. Based on proxy records, the timing of gLGM is constrained
45 between 26.5 to 19 ka, during which the ice sheets and mountain glaciers reached their maximum and the global sea
46 level was at its minimum (Clark et al., 2009).

47 The timing and extent of the maximum glaciation in many regions are still poorly understood and may differ
48 from one region to another in due to distinct ice masses respond differently to local and regional climatic conditions.
49 However, new geochronological techniques such as in situ cosmogenic surface exposure dating (e.g., Heyman, 2014;
50 Hughes et al., 2013) permit reliable temporal comparisons between the maximum advances of different mountain
51 glaciers.

52 Evidence from mid-latitude glaciers reveals a more complex behavior than that of synchronized ‘global’
53 glaciations. In some parts of central Asia, for example, the largest glacial extent occurred before MIS 2, > ~100 ka in
54 the northeastern Tibetan plateau (Heyman et al., 2011a) and late MIS 5/MIS 4 in the Kanas lake, Chinese Altay
55 (Gribenski et al. 2018). In the Tian Shan (Blomdin et al., 2016; Li et al., 2014; Koppes et al., 2008), Altay (Blomdin
56 et al., 2018), Khangay (Batbaatar et al., 2018; Pötsch, 2017; Smith et al., 2016; Rother et al., 2014), and Eastern Sayan
57 (Batbaatar and Gillespie, 2016; Gillespie et al., 2008) mountains of the central Asia, the largest glaciers dated to MIS
58 3, while the MIS 2 glaciers appeared to be smaller. It is noteworthy that most of the MIS 3 advances are based on a
59 few and/or widely scattered ages of moraine boulders (Gribenski et al., 2018; Blomdin et al., 2016). On the other hand,
60 in the Gichgene range with arid climate conditions, the significant cirque glacier advanced during MIS 1 (Batbaatar
61 et al., 2018). These studies suggest that glaciers in continental central Asia respond to regional-scale climate
62 fluctuation in different ways; hence, the last glacial maxima differed from place to place on a scale of a few hundred
63 kilometers from the arid to humid continental environments.

64 In addition to regional climate conditions, non-climatic factors may also control the local extent and dynamics
65 of glaciation. Topographic factors such as catchment morphology, valley width, length, slope, and aspect, can
66 influence glacier dynamics and affect the style of glaciation (Barr and Lovell, 2014; Kirkbride and Winkler, 2012).
67 Glacier mass balance varies with slope aspect, snow avalanche, and wind drifting snow. Particularly, the north-south
68 aspect contrast in mid-latitude regions with steeper slopes, higher relief, and higher insolation can generate substantial



69 differences in insolation and melt. This difference may be more significant for cirque, small mountain glaciers, or
70 niche glaciers than for large valley glaciers or ice caps (Evans and Cox, 2005).

71 Although spatio-temporal variations in the glacial extent in response to regional climate change have been
72 mentioned in numerous studies, the influence of topographic changes has not been adequately explored. The present
73 study aims to reconstruct the glacier extent and chronology of major glacial events during the last glacial cycle in
74 previously unstudied Ih Bogd massif of southwestern Mongolia. Our original hypothesis was the north and south
75 facing valleys would experience synchronous paleoglacial advances. Upon falsifying this hypothesis using ¹⁰Be
76 surface exposure dating, we then turned to a 2D glacier surface model to determine if the impact of aspect could have
77 influenced the chronology for two contrastively oriented (north-facing and south-facing) valleys.



78 **2. STUDY AREA**

79 **2.1 Geology**

80 The Gobi-Altay range, a ~800 km long NW-SE trending isolated arc of mountains, is bordered in the northwest by
81 the Mongolian Altay range and separated from the Khangay range by Gobi Lakes Valley. Ih Bogd massif (Ih Bogd
82 means ‘great saint’ or ‘great sacred mountain’ in Mongolian) is located in the northern Gobi-Altay range. Its position
83 in the heart of the Gobi makes it an important site to understand the extent and timing of glacial changes in arid central
84 Asia.

85 This massif is over 50 km long, 25 km wide, and rises ~2 km above the surrounding arid piedmont. The
86 highest peak of the massif, Terguun Bogd (3957 m a.s.l), is the highest point of the Gobi-Altay Mountain range as
87 well (Fig. 1). A sequence of thrust faults and sinistral strike-slip faults, which together form transpressional pop-up
88 structures, govern the current stress regime of Ih Bogd (Vassallo et al., 2011; Vassallo et al., 2007; Bayasgalan et al.,
89 1999; Cunningham et al., 1996). The highest part (>3000 m) of the flat summit plateau consists mainly of Mesozoic
90 granite, while lower parts are mostly occupied by Cenozoic gneisses (Vassallo et al., 2011; Jolivet et al., 2007;
91 Tomurtogoo, 1999).

92 The flat summit plateau is thought to be a remnant of a formerly extensive Mesozoic erosion surface (Jolivet
93 et al., 2007; Devyatkin, 1974; Berkey and Morris, 1924), surviving most of the Cenozoic due to its rapid and recent
94 uplift after long-term quiescence (Jolivet et al., 2007). Accordingly, erosion in Ih Bogd is limited to several deep
95 gorges. The summit plateau is well-preserved in unincised areas because of the young age of the massif and arid
96 regional climate (Vassallo et al., 2011).

97

98

99 **2.2 Climate**

100 Ih Bogd massif is situated in the cold Gobi Desert, having a high amplitude in diurnal and annual temperatures.
101 The climate of the study area is characterized by a dry, cold winter with limited snowfall and hot summer with more
102 than 65% annual precipitation coming in summer (Batbaatar et al., 2018). Bayankhongor (Fig. 2), the nearest aimag
103 center (the largest unit of the Mongolian province) is 140 km distant and receives less than 200 mm of precipitation
104 per year (188 mm, an average of 2005–2019, NAMEM, 2020), while precipitation reaches ~100 mm (Yu et al., 2017,
105 Fig. 2b, 2c and 2d) near Orog lake (1168 m a.s.l, Zhang et al., 2022). The closest weather stations to Ih Bogd are
106 Bayangobi (1540 m a.s.l) in the south and Bogd (1240 m a.s.l) in the north. The long-term mean annual temperature
107 measured as 3.1 °C in Bayangobi and 4.4 °C in Bogd (Fig. 2c and 2d). The average January temperature was
108 approximately -18 °C in both stations (NAMEM, 2020).

109 In the adjacent Gobi Lakes Valley, starts to snow at the end of September but melts rapidly. However, a thin
110 snow cover persists on the summit plateau of Ih Bogd between the end of September and the middle of April.
111 Sometimes, precipitation falls as snow from June to August (Landsat imagery, Farr et al., 2007). On the other hand,
112 summer is warm and wetter. The July temperature rises to about 21.8 °C in Bayangobi and 23.0 °C in Bogd (Fig. 2d;
113 NAMEM, 2020).



114 Ih Bogd has a long-living snow cover, lower mean annual temperature (-10°C), and receives more
115 precipitation (~ 200 mm) than its surrounding (Fig. 2a, 2b). Strong Siberian high pressure prohibits the entrance of
116 westerlies during winter, while westerlies and southwesterlies are still effective during summer time in the study
117 region. The orientation and shape of mobile dunes northwest of Orog lake record the prevailing winds as being from
118 the northwest (Mischke et al., 2020; NAMEM, 2020; Yu et al., 2019).

119

120 **2.3 Glacial landforms and study site setting**

121 The Ih Bogd massif contains abundance well-developed alpine glacial erosional landforms such as cirques,
122 valleys and depositional landforms such as lateral, terminal and recessional moraine ridges, glacial tills on its northern
123 and southern slopes. Headwater systems of intermittent streams merge and turn into main streams, which later flow
124 out of the mountain front as large alluvial fans. The sediment transported by alluvial fan or intermittent streams
125 accumulates in large endorheic intermontane basins like Gobi Lakes Valley (Fig. 2). Our particular interest in the
126 present study is to compare the timing of the largest glacier extent in the two small paleo valley glaciers flowed to the
127 south (Ih Artsan) and the north (Jargalant; Fig. 1).

128 Glaciers in both valleys were started from cirque shaped headwater above ~ 3100 m and flowed down to
129 elevations of ~ 3000 – 3200 m. Jargalant valley merge down to the largest valley on the northern flank called Bituut
130 river valley. This large drainage only experienced glaciations in the form of short cirque-valley glaciers on its
131 headwaters, like in Jargalant valley. A few well-preserved moraine ridges have been previously identified near the
132 headwater of Bituut river (Batbaatar et al., 2018). The massif was limited to small cirque-valley glaciers is best
133 explained by the arid climate of the interior of the Gobi Desert.



134 **3. METHODOLOGY**

135 **3.1. Field investigation and geomorphologic mapping**

136 We conducted the fieldwork in July of 2018 riding horses. Prior to fieldwork, glacial extent and moraine ridges were
137 pre-analyzed in a GIS environment and mapped on 30 m Shuttle Radar Topographic Mission (SRTM), ALOS
138 PALSAR DEM with 12.5 m resolution (JAXA/METI, 2007), and Landsat 8 imagery with one arc-second resolution
139 (Roy et al., 2014; Farr et al., 2007). Names of the study areas and physical characteristics of the specific landforms
140 were identified from a 1:100000-scale topographic map of Mongolia (NAGC, 1969) using their morphology and
141 depositional properties. Pre-identified moraines were confirmed during fieldwork. They were then categorized based
142 on their stratigraphic position, morphology, and weathering traits.

143

144 **3.2. Moraine morphostratigraphy**

145 As indicated previously, late Quaternary moraines are only preserved in headwaters. Ih Artsan cirque is smaller and
146 glacial valley is shorter (~ 1 km) than Jargalant. The best-preserved moraines, with at least seven to eight morainal
147 crests, occur in the Ih Artsan cirque (Fig. 3; Batbaatar et al., 2018). The farthest moraine sequence (M_{Ih1}) from the
148 summit plateau was distinguished by abundant matrix-rich glacial sediments, large granitic boulders, and a bulge-like
149 moraine ridge higher than the inner moraine crests (Fig. 3).

150 The Jargalant paleoglacier has a larger accumulation area and length than Ih Artsan glacier, advancing 1.5
151 km downvalley. Stratigraphically, we identified four different moraine sequences in the Jargalant complex: M_{J4} , M_{J3} ,
152 M_{J2} , M_{J1} (from youngest to oldest). M_{J4} moraine lies between 3365–3410 m a.s.l, containing angular to sub-angular
153 clast supported pebble to boulders. Downvalley from M_{J4} moraine, M_{J3} and M_{J2} moraines have smooth matrix-
154 supported flat tops and steep clast supported sides. These sequences are longitudinally dissected by intermittent
155 streams draining toward Bituut valley. The oldest moraine (M_{J1}) was deposited further downvalley, consisting of a
156 bulging morainal form with large granitic boulders lying on the finer matrix-supported deposit. We speculate that this
157 oldest preserved material might have extended far enough to reached the Bituut valley (trunk valley). The sequences
158 were very clearly distinctive in the field as well as in the satellite images (Fig. 4; Fig. 5b).

159

160 **3.3. Equilibrium Line Altitude**

161 Ih Bogd massif is unglaciated today. Furthermore, the nearest modern glaciers are glaciers in Otgontenger (Khangay),
162 Sutai (Mongolian Altay), which are approximately 350 to 550 km west of the study area. Thus, we could not calculate
163 present ELAs or ELA depression; hence only ELAs for former glaciers were estimated.

164 The THAR method may include a large error when glacier geometry is complex (Benn & Lehmkuhl 2000).
165 Yet, it is more suitable for our study area because it has simple glacier morphology. In this study, we obtained the
166 altitude of the lower and upper limit of past glaciers using GPS, Google Earth imagery, and an ALOS PALSAR DEM
167 with 12.5 m resolution (JAXA/METI, 2007). The glacial toe was considered to be the minimum altitude of the terminal
168 moraine, while the glacial headwall altitude was considered to be 1/3 of the altitude difference between the cirque
169 floor and top of the rock cliff (Goldthwait, 1970). Estimates of the headwall altitude for high and steep cirques can
170 range from tens to hundreds of meters, and determination of the glacial headwall is elusively subjective and arbitrary



171 (Porter 1981). The median altitude method (MEM; THAR=0.5) is commonly used; however, according to glacier type
172 or location, lower (Meierding 1982) or higher (Gillespie et al. 2008) ratios may be used. For this reason, we also used
173 a higher THAR ratio of 0.58 (Gillespie et al. 2008) because Ih Bogd massif must have higher ratio due to its arid
174 environment during the last glaciation (Lehmkuhl et al., 2018; Felauer et al., 2012).

175

176 **3.4. Cosmogenic ^{10}Be surface exposure dating**

177 We used cosmogenic ^{10}Be surface exposure dating based on the specific sampling procedure below to determine the
178 timing of the last glacial advances in Ih Bogd massif (Khandsuren et al., 2019; Gosse and Phillips, 2001). We sampled
179 quartz-rich granitic boulders on the moraine crests, which were not reworked and represented single, distinguishable
180 ice-marginal positions. We sampled boulders that are rooted in the upper flat surface of the moraine crest and away
181 from steep slopes to avoid post-depositional movement such as rolling and sliding downslope. We avoided boulders
182 smaller than 50 cm above ground level that are likely to have been buried, exhumed, or heavily eroded. Samples were
183 obtained by chisel and hammer from the top surfaces of boulders (less than 5 cm thick) to avoid the edging effect. We
184 sampled at least five boulders from each single moraine crest to statistically screen any outliers such as inheritance or
185 post-glaciation reworking.

186 We followed the laboratory works of Korea University Geochronology Laboratory (Seong et al., 2016), with
187 the revised procedure of Kohl and Nishiizumi (1992). Rock samples were crushed and sieved to obtain a
188 monomineralic quartz sample and avoid grain size dependency. Meteoric ^{10}Be and other contaminations were removed
189 by successive HF/HNO₃ leaching. Purified quartz samples (250~500 μm) were first spiked with ~1047.8 ppm
190 concentrated ^9Be carrier and then dissolved with HF/HNO₃. Fluorides were removed by Perchloric (HClO₄) acid,
191 while Be was separated from other ions (cations/anions) using ion-exchange chromatography columns. Beryllium
192 hydroxide was recovered using ammonium hydroxides. Consequently, Be(OH)₂ gels were dried at high-temperature
193 hotplates. They were calcinated to be oxide forms in a furnace at higher temperatures (800 °C). BeO samples were
194 mixed with Niobium powder to get conductivity and targeted in aluminum target to be loaded into 6 MV tandem
195 Accelerator Mass Spectrometry (AMS) for $^{10}\text{Be}/^9\text{Be}$ ratio measurement in the Korea Institute of Science and
196 Technology. $^{10}\text{Be}/^9\text{Be}$ ratios for each sample were measured relative to the 07KNSTD standard sample 5-1
197 (Nishiizumi et al., 2007), having a $^{10}\text{Be}/^9\text{Be}$ ratio of $2.71 \times 10^{-11} \pm 4.71 \times 10^{-13}$ (calibrated error). The measured average
198 ^{10}Be to ^9Be ratio of the processing blank was $4.53 \times 10^{-15} \pm 1.6 \times 10^{-15}$ (n=2). The exposure ages were calculated using
199 Cronus-Earth online calculator v3 (Balco et al., 2008). ^{10}Be Production rate scaling was based on the time-dependent
200 and nuclide-specific LSDn scaling (Lifton et al., 2014) as well as the non-time-dependent scaling model (Stone, 2000).
201 Errors of exposure ages were represented by external uncertainty (1σ confidence level). We tested the boulder
202 populations for finding outliers using the Chauvenet and Pierce criterion and normalized deviation methods (Ross,
203 2003; Chauvenet, 1960) before we assigned deglaciation ages of moraine sequences. For the normalized deviation, a
204 sample in populations was rejected if its normalized deviation from the group mean (excluding the tested sample) was
205 greater than two (Batbaatar et al., 2018). We also calculated the reduced chi-square value and the relative uncertainty
206 of the group (Blomdin et al., 2018). The arithmetic mean and standard deviation (1σ) of the exposure ages in the group
207 was considered as a representation of the age. We assumed zero erosion for all samples because it has been negligible



208 (at least for the sampled surface) since the boulders were deposited, based on field observations. We omitted
209 corrections for snow cover and vegetation change due to the ephemeral winter snow cover at the elevations of the
210 sampled boulders (e.g., Gosse and Phillips, 2001) because modern winter snow cover (Oct-Apr) is very thin and no
211 tree cover exists due to aridity.



212 **4. RESULTS**

213 **4.1. Late Pleistocene ELA reconstruction**

214 LGM ELA was calculated for M_{Ih1} and M_{J1} moraines (Table 1). We estimated the former ELA using a headwall
215 altitude of 3508–3532 m. The terminal moraine was also identified at an elevation of 3222 m a.s.l in the Ih Artsan
216 valley. Accordingly, the ELA for the M_{Ih1} moraine was 3388 m a.s.l. In contrast, a large terminal moraine was
217 deposited at 2998 m a.s.l in Jargalant valley. The ELA associated with M_{J1} moraine was 3308 m a.s.l., about 80 m
218 lower than M_{Ih1} moraine.

219

220 **4.2. ^{10}Be surface exposure age dating**

221 We present the new $28\ ^{10}\text{Be}$ exposure ages obtained from the boulders associated with five different moraine sequences,
222 M_{Ih1} in Ih Artsan valley and M_{J1} , M_{J2} , M_{J3} , and M_{J4} sequences in Jargalant (Table 2; Fig. 5).

223 **Ih Artsan valley:** seven granitic boulders (IAM001–007) collected from the most distal moraine ridge ranged in age
224 between 21.2 ± 1.5 to 19.1 ± 1.3 ka. ^{10}Be exposure ages from this moraine sequence were well clustered, and no outlier
225 was detected, yielding a group mean of 20.1 ± 0.7 ka. $R\chi^2$ was 0.29, and group relative uncertainty was calculated as
226 4% (Fig. 6).

227 **Jargalant valley:** twenty-one granitic moraine boulders on the four moraine sequences were collected. Five to seven
228 boulders from each moraine crest were sampled. Exposure ages from the innermost M_{J4} moraine ranged from 636.2
229 ± 45.1 to 177.3 ± 11.3 ka. The oldest age (JAM003, 636.2 ± 45.1 ka) was excluded, and the four remaining ^{10}Be
230 exposure ages provided a mean age of 212.9 ± 45.9 ka. Five boulders from the M_{J3} moraine ranged in age between
231 209.0 ± 26.1 to 35.9 ± 8.0 ka. Group mean age was calculated as 69.9 ± 39.4 ka after rejecting an outlier of $209.0 \pm$
232 26.1 ka (JAM008). Boulders from the M_{J2} moraine yielded ages from 284.9 ± 18.4 to 162.1 ± 10.2 ka with a mean
233 exposure age of 193.7 ± 36.7 ka after rejecting the oldest age of 284.9 ± 18.4 ka (JAM012). Samples from the distal
234 moraine of Jargalant valley (M_{J1}) ranged in age from 18.9 ± 1.7 to 10.6 ± 0.8 ka. The arithmetic mean age for this
235 moraine sequence was 17.2 ± 1.5 ka without the youngest age of 10.8 ± 0.5 ka (JAM016). Group was relatively well
236 clustered, and its relative uncertainty was 9% and $R\chi^2 = 1.18$ (Fig. 6).

237 Boulders from inner moraines (M_{J4} , M_{J3} , M_{J2}) presented older (~ 636.2 – 35.9 ka) exposure than the timing of
238 the maximum extent unlike morphostratigraphy—the inner moraines should be younger than the distal moraine (M_{J1}).
239 We interpret that the unexpected older exposure ages (~ 636.2 – 35.9 ka) from M_{J4} , M_{J3} , M_{J2} moraines of Jargalant
240 valley strongly imply the inheritance from the summit plateau. These unusually old boulders are pieces of the summit
241 plateau that were transported onto the glacier surface by rockfall as the cirque walls were undermined by growing ice,
242 which seems to happen in the recent times as well (Table 2; Fig. 5b). The unexpected, significant inheritance has been
243 widely recognized around the globe in the literature of cosmogenic nuclides dating (Ciner et al., 2017; more references
244 therein), possibly overestimating the real age of moraine.

245



246 5. THE 2D ICE SURFACE MODELLING: METHODS AND RESULTS

247

248 Our original hypothesis was that the north and south-facing cirques of the Ih Bogd massif would be
249 concordant. The results were that the glaciers on the opposite aspects were asynchronously behaved, by about 3
250 millennia. These findings led to a second hypothesis, that aspect might provide enough of a difference to explain the
251 asynchrony. Thus, to stay true to the research events, we combine methods and results of simulating a simple 2D ice
252 surface model including mass balance calculation covering the time period of 22–16 ka. Our exercise cannot simulate
253 actual glaciers, however, rather simply assess the idea that aspect might produce enough of a difference in mass
254 balance and ice surface via different melt rates to explain the empirical dating results.

255

256 5.1. Glacial surface mass balance model

257 Glacier mass balance (m) is determined by the summation of net accumulation (c) and ablation (a) over a stated period
258 (t):

$$259 \quad m = c + a = \int_{t_1}^{t_2} (c + a) dt \quad (1)$$

260 To infer the net gain and loss of glacier mass along the longitudinal profile (Fig. 7a, b, c) for both catchments, we
261 calculated and plotted the variations in summer (JJA) mean melt rate and winter precipitation (i.e., snow in the whole
262 year) during 22-16 ka ago. Site parameters and input parameters of this model are described in Tables 3 and 4.

263

264 5.1.1 Temperature-index glacier melt model including potential clear-sky direct solar radiation

265 We calculated time-dependent incoming solar radiation of the study area by applying the potential clear-sky direct
266 solar radiation method to a 12.5 m resolution DEM to realize the aspect effect on insolation distribution in mountainous
267 areas. For simplicity, we rerun this insolation model along a longitudinal profile line drawn for Ih Artsan and Jargalant
268 glacial valleys (Fig. 7). Subsequently, we combined the insolation values with the temperature index melt model. To
269 calculate melt, we used a series of equations in the following steps, calculating: 1) orbital parameters; 2) topography;
270 3) hour angle on an arbitrary inclined surface and day length; 4) local zenith angle and angle of incidence with hour
271 interval; 5) hourly insolation; 6) integrate hourly insolation into daily insolation; 7) daily melt; and 8) summer (JJA)
272 melt integration for given time of interval (22-16 ka).

273 The earth's rotation around its axis causes the diurnal changes in incoming solar radiation; the position of
274 this axis relative to the sun causes seasonal changes; the variations in eccentricity, axial tilt, and precession cause
275 combined to result in long-term cyclical changes in climate. Correspondingly, two main orbital parameters, solar
276 declination (δ) and eccentricity correction factor ($R_m R^{-1}$)² were used for the calculation of the further paleo solar
277 radiation for 22-16 ka (Berger and Loutre, 1991).

278 According to the aspect effect, north-facing slopes must receive less direct solar radiation than south-facing
279 slopes in the mid-latitude northern hemisphere. To define aspect-driven contrast in potential direct solar radiation
280 between south-facing and north-facing valleys, we applied the same input parameters, except for the topography
281 (aspect and slope). Sunrise and sunset hour angles on the inclined surface were calculated as a function of latitude,
282 solar declination, slope, and azimuth (Iqbal, 1963).



283 Sunrise hour angle for horizontal surface:

$$284 \quad \omega_s = \cos^{-1} (-\tan\phi \tan\delta) \quad (2)$$

285

286 To obtain hour angles on the inclined surface, x and y were extracted from formula 1.6.7 created by Iqbal (1963).

$$287 \quad x = \frac{\cos\phi}{\sin\gamma \tan\beta} + \frac{\sin\beta}{\tan\gamma} \quad (3)$$

288

$$289 \quad y = \tan\delta \left(\frac{\sin\phi}{\sin\gamma \tan\beta} - \frac{\cos\phi}{\tan\gamma} \right) \quad (4)$$

290

291 The following equations give the sunrise and sunset hour angles on the surface oriented toward the east.

$$292 \quad \omega_{sr} = \min \left[\omega_s, \cos^{-1} \left(\frac{-xy - \sqrt{x^2 - y^2 + 1}}{x^2 + 1} \right) \right] \quad (5)$$

293

$$294 \quad \omega_{ss} = -\min \left[\omega_s, \cos^{-1} \left(\frac{-xy + \sqrt{x^2 - y^2 + 1}}{x^2 + 1} \right) \right] \quad (6)$$

295

296 The following equations give the sunrise and sunset hour angles on the surface oriented toward the west.

$$297 \quad \omega_{sr} = \min \left[\omega_s, \cos^{-1} \left(\frac{-xy + \sqrt{x^2 - y^2 + 1}}{x^2 + 1} \right) \right] \quad (7)$$

$$298 \quad \omega_{ss} = -\min \left[\omega_s, \cos^{-1} \left(\frac{-xy - \sqrt{x^2 - y^2 + 1}}{x^2 + 1} \right) \right] \quad (8)$$

299 Equations 2 to 8 are for calculating hour angles in arbitrary surfaces, where ω_s is the sunrise hour angle for
300 horizontal surfaces, ω_{sr} , ω_{ss} is the sunrise and the sunset hour angles on the inclined surface, ϕ is the latitude, δ is the
301 solar declination angle, β is the slope inclination angle, and γ is the surface azimuth angle.

302 Furthermore, the local zenith angle (Z) and the angle of incidence (θ) were calculated using a one-hour
303 interval of hour angle (ω). The zenith angle is approximated as a function of latitude, solar declination angle, and hour
304 angle (Iqbal, 1983):

305

$$306 \quad Z = \sin\delta \sin\phi + \cos\delta \cos\phi \cos\omega \quad (9)$$

307

308 and the angle of incidence on the arbitrary oriented surfaces is expressed as:

309

$$310 \quad \cos\theta = (\sin\phi \cos\beta - \cos\phi \sin\beta \cos\gamma) \sin\delta + (\cos\phi \cos\beta + \sin\phi \sin\beta \cos\gamma) \cos\delta \cos\omega + \cos\delta \sin\beta \sin\gamma \sin\omega$$

$$311 \quad (10)$$

312

313 where β is the slope inclination angle and γ is the surface azimuth angle.

314 Hourly potential clear-sky direct solar radiation (I) during daytime is calculated as (Hock, 1999):

$$315 \quad I = I_0 \left(\frac{R_{mn}}{R} \right)^2 \Psi_a \left(\frac{P}{P_0 \cos Z} \right) \cos\theta \quad (11)$$



316 where I_0 is solar constant (1368 W m^{-2}), $(R_m/R)^2$ is the eccentricity correction factor of the Earth's orbit for the time
 317 considered with R the instantaneous Sun-Earth distance, and R_m is the mean Sun-Earth distance, Ψ_a is the mean
 318 atmospheric clear-sky transmissivity ($\Psi_a=0.75$: (Hock, 1998)), P_h is the atmospheric pressure (OAF, 1976), P_0 is the
 319 mean atmospheric pressure at sea level, Z is the local zenith angle, and θ is the angle of incidence between the normal
 320 to the grid slope and the solar beam. Daily solar radiation resulted from integration of hourly solar radiation for each
 321 day

322

323 We calculated daily melts with equation (12) and integrated them into annual summer melt.

324

$$325 \quad a = \begin{cases} \left(\frac{1}{n}MF + a_{\text{ice}}I\right)T & : T > 0 \\ 0 & : T \leq 0 \end{cases} \quad (12)$$

326 MF is a melt factor ($\text{mm d}^{-1} \text{ } ^\circ\text{C}^{-1}$), a_{ice} is a radiation coefficient for ice surfaces, I is potential clear-sky direct solar
 327 radiation at the ice surface (W m^{-2}), and T is the monthly mean temperature ($^\circ\text{C}$).

328

We calculated the paleotemperature of the study area in the following order.

329

330 1st) Present-day monthly air temperatures (T) for both cirque headwall altitudes (3533.3 m in Jargalant, 3508.3 m in
 331 Ih Artsan) were calculated from the two nearest national weather stations using a summer adiabatic lapse rate of $8 \text{ } ^\circ\text{C}$
 332 km^{-1} (Batbaatar et al., 2018). Bayangobi weather station locates (1540 m a.s.l) $\sim 27 \text{ km SE}$ and Bogd (Horiult) weather
 333 station (1240 m a.s.l) is $\sim 45 \text{ km NE}$ from the study area (Fig. 2c).

333

334 2nd) We use only summer temperature because even today, monthly mean temperatures between August to May are
 335 less than $0 \text{ } ^\circ\text{C}$, in which no melt occurs (NAMEM, 2020). Present-day precipitation falls as snow between the end of
 336 September to the middle of April. Sometimes it snows even in summer (Landsat imagery, Farr et al., 2007). The
 337 summer mean temperature (JJA) at the cirque headwall altitude was measured as $3.5 \text{ } ^\circ\text{C}$ in Jargalant valley and $5.4 \text{ } ^\circ\text{C}$
 338 in the Ih Artsan valley. We chose the value of $5.4 \text{ } ^\circ\text{C}$ for the summer temperature of the study area and used further
 339 calculations (see supplementary 1 file).

339

340 3rd) We obtained a time-dependent summer temperature since 22 ka. LGM summer temperature was easily calculated
 341 by subtracting known LGM summer temperature anomaly ($1\text{--}7 \text{ } ^\circ\text{C}$ by Tarasov et al., 1999) from the present-day
 342 temperature of the study area. The study area's present-day and LGM summer temperature was calibrated to Greenland
 343 temperature data (from NGRIP ice core) since 22 ka (Buizert et al., 2018) to obtain time-dependent temperature
 344 variation (see supplementary 2 file).

344

345 4th) LGM summer temperature anomalies ranging from $-5.0 \text{ } ^\circ\text{C}$ to $-6 \text{ } ^\circ\text{C}$ were applied to calculate glacial melt since
 346 22 ka (see supplementary 2 file).

346

347 5.1.2. Glacier accumulation and snow data

348

349 Climatologies at high resolution for the earth's land surface areas (CHELSA) provides a high resolution, downscaled
 350 centennial climate model data since 20 ka. We used CHELSA-TraCE21k 1 km monthly precipitation time series
 (Karger et al., 2021). Precipitation data between 22–20 ka was considered the same as 20 ka data. Only snowfall at



351 the mean altitude of each valley was considered glacial accumulation, which occurs when the monthly average
352 temperature is below 0 °C.

353

354 **5.2. 2D ice surface model based on glacier thickness change**

355 Finally, a simple 2D ice surface model reconstructed paleo glacier behavior from 22–16 ka in the study area. First, we
356 created small initial glacial surface profiles on both valleys using the 2D ice surface model developed by Benn and
357 Hulton (2010). The model calculates the ice surface elevation (ice thickness) along the profiles (Fig. 7a, b, c) in both
358 valleys. The model only requires an input of the yield stress that is assumed to describe a glacier's basal shear stress
359 regime and a shape factor accounting for the valley-drag effects. We plot the ice profile with 5 m spacing, assuming
360 constant basal shear stress of 50, 100, 150, 200, and 300 kPa. According to the glacial valley scale and paleoglacier
361 extent, we chose the higher basal shear stress of initial glacier for Jargalant valley (200 kPa) and the smaller value for
362 Ih Artsan valley (100 kPa). Shape factors were calculated perpendicular to the profile at intervals of 5 m. Subsequently,
363 we calculated the glacier mass balance for 22–16 ka using our temperature-index melt model results and paleo snow
364 accumulation data. Therefore, we applied corresponding paleo mass balance values on the initial ice thickness profiles.
365 A cross-section of the thickest ice was recognized as ELA. Accordingly, paleo ELAs were calculated regarding the
366 ice thickness change. Eventually, we used the simple quadratic function formula ($f(x)=ax^2 + bx + c$) to determine the
367 location of the glacial toe based on ELA and headwall altitude values (Benn and Hulton 2010). With the glacial toe
368 location, we could evaluate the paleoglacier advance and retreat at any time of interest.

369

370 **5.3. 2D Ice surface modelling result**

371 We ran the potential direct solar radiation model applying to a 12.5 m resolution DEM for a more realistic
372 comparison. The model suggests that the aspect largely affects the incoming potential clear-sky solar radiation. The
373 result approved that the south-facing slopes in mountainous regions receive more significant solar radiation than the
374 north-facing slope in the northern hemisphere. According to the exact orientation (aspect) of the valleys (northeast to
375 southwest), hourly maximum insolation in Ih Artsan and minimum insolation in Jargalant were observed between 15
376 to 16 o'clock, not at noon. The present-day June solstice incoming daily solar radiation was 8527.34 WH m⁻² in Ih
377 Artsan valley and 7714.35 WH m⁻² in Jargalant valley but the solar radiation was smaller in 22 ka, 8460.07 WH m⁻²
378 in Ih Artsan, and 7604.54 WH m⁻² in Jargalant. Although both valleys received maximum insolation in the first to
379 middle half of June, the maximum difference in incoming daily solar radiation occurred at the end of August. The
380 main difference in the daily incoming solar radiation ranges from 10–24% in summer days over 22–16 ka. The spatial
381 distribution of potential direct solar radiation of the study area is given in Fig. 7. Typically, total daily insolation of
382 summer solstice for 20 ka (Fig. 7a), summer insolation for thousand years (21–20 ka), and total summer insolation
383 over 22–16 ka was described on the 12.5 m grid cells. In the same way, 14% excess of total summer insolation was
384 observed on the southern slope during over modelling time interval of 22–16 ka (Fig. 7b, c, see supplementary 2 file).

385 For simplicity, the melt was calculated along valley profile of Ih Artsan and Jargalant valleys (Fig. 7). In
386 accordance with the incoming solar radiation contrast, melt rates on south-facing slopes exceed those on north-facing
387 slopes, as would be expected. If modern glaciers existed in Ih Bogd, the present-day summer melt would be calculated



388 as 4.02 m in Jargalant valley and 3.7 m in Ih Artsan valley, respectively. This was a substantially higher melt rate in
389 the arid, cool climate of the study area. The temperature-index melt model discovered that 5% of melt excess in June
390 solstice of any year between 22–16 ka was observed on the south-facing slope. Approximately 8% of the difference
391 in summer melt in any year was observed during 22–16 ka (Fig. 7, see supplementary 2 file)

392 Except for the present-day temperature and topographic data, the same input parameters were applied to both
393 valleys. LGM summer temperature anomalies ranging from -6 °C to -5 °C with 0.1 °C intervals were applied the same
394 for both glaciers. We used input parameter of 100 kPa of basal shear stress for Ih Artsan initial glacier (22 ka), while
395 a twofold value (200 kPa) for Jargalant in proportion to the size of the glaciers. We applied two different present-day
396 temperature values for the Jargalant glacier, but LGM summer temperature anomalies were the same for both cases.
397 We ran the 2D ice surface model from 22 ka to 16 ka with two cases according to the different temperature inputs: 1)
398 using the same present-day temperature; and 2) using the different present-day temperature for both valleys.

399 **Case 1.** Applying the same present-day temperature: The timing of maximum extent was similar for both
400 valleys when using the same site temperature. When we give LGM anomaly -5.5 °C, the timing of the maximum
401 extents (20.23 ka) for both valleys were consistent with the Ih Artsan terminal moraine age dating result (20.1 ka).

402 **Case 2.** Applying the different present-day temperatures: For the Jargalant glacier, we applied lower present-
403 day temperature by -1 °C to -0 °C (at 0.1 °C interval) than Ih Artsan. The run yielded different chronologies of
404 maximum ice expansions. The gaps between maximum ice advance timings range from 2.70–3.46 kyr. When we
405 applied -5.5 °C of LGM summer temperature anomaly and present-day summer temperature in Jargalant 0.5 °C lower
406 than in Ih Artsan, Ih Artsan glacier reached its maximum extent near 20.23 ka. In contrast, the Jargalant glacier
407 maximally advanced approximately at 17.13 ka. This result perfectly fits our ¹⁰Be moraine age dating results (20.1 ka
408 and 17.2 ka).



409 **6. DISCUSSION**

410

411 **6.1. Asynchrony in LGM ice expansion across the western Mongolia**

412 Our study shows the glaciers of Ih Artsan valley reached its maximum extent during gLGM at 20.1 ± 0.7 ka.
413 Several inner moraine ridges (Fig. 5a) were recognized and some of them dated to 15–13 ka (Batbaatar et al., 2018).

414 In the other hand, our study also documents the farthest found moraine (M_{J1}) in Jargalant valley formed
415 around 17 ka (17.2 ± 1.5 ka), three millennia later than the south-facing Ih Artsan valley. We could not find any other
416 evidence that the Jargalant glacier reached the trunk valley of Bituut river. Probably geological markers could have
417 been erased by the main river of Bituut or earlier advances were less extensive. However, we suggest the exposure
418 age (17.2 ± 1.5 ka) of the distal moraine (M_{J1}) is the age for maximum extent for the Jargalant valley (Fig. 5b and 6),
419 because this moraine was not like the small ridge left as a glacier stagnates during its retreat. The M_{J1} moraine was
420 larger than the other moraine sequences, large enough to mark the maximum advance of the glacier.

421 Some ^{10}Be exposure ages of the glacial erratic from the mountain ranges nearby Ih Bogd show the significant
422 glacial advances between LGM to the Holocene (Fig. 8). The largest ice extent was dated as ~ 22.0 ka on the western
423 flank of the Sutai (Batbaatar et al., 2018). On the other hand, the farthest ice expansion corresponds to MIS 3 in the
424 Khangay mountain range (Batbaatar et al., 2018; Pötsch, 2017; Smith et al., 2016; Rother et al., 2014). In the Gichgene
425 mountains, Holocene (8–7 ka) glaciers advanced with a similar magnitude to their local LGM position. Generally, two
426 main glacial stages, LGM and post LGM (~ 17 – 16 ka), were observed within MIS 2 in Mongolia (Batbaatar et al.,
427 2018; Pötsch, 2017; Batbaatar and Gillespie, 2016; Smith et al., 2016; Rother et al., 2014).

428 A suite of granulometric, palynological, ostracod, and geochemical proxies from the Gobi Lakes Valley
429 reveal several harsh and dry climates, including the local LGM (19–18 ka) and Younger Dryas (Mischke et al., 2020;
430 Yu et al., 2019; Lehmkuhl et al., 2018; Yu et al., 2017; Lee et al., 2013; Felauer et al., 2012, Fig. 8). Abrupt
431 deglaciation occurred near 20 ka in Ih Artsan valley, whereas the lower boundary of deglaciation likely began at 17.2
432 ka on Ih Bogd's northern slope (Jargalant). The warming trend was also present in the Gobi Lakes Valley, where lakes
433 once were desiccated during local LGM, and experienced water level increase after local LGM (e.g., Mischke et al.,
434 2020; Yu et al., 2017).

435

436 **6.2. Asynchronous LGM glaciation in other mid-latitude ranges**

437 Recent glacial chronologies from mid-latitude mountain ranges in North Atlantic region document that Laurentide,
438 Scandinavian ice sheets and number of valley glaciers behaved synchronously, advancing to their maximum extent at
439 roughly the same time as the gLGM (26.5–19 ka). However, some experienced pre-LGM glacial maxima, while others
440 stagnated, re-advanced, continuously advanced even farther during the subsequent Heinrich Stadial 1 (HS-1, 17.5–
441 14.5 ka), displaying both inter-range and intra-range asynchrony (Palacio et al., 2020; Licciardi and Pierce 2018;
442 Young et al., 2011, Laabs et al., 2009).

443 Large scale inter-range asynchrony (several tens of kyr) of last glacial termination was common in Europe.
444 Cosmogenic surface dating from Alps and Turkey provides nearly synchronous last glacial maxima with the gLGM
445 (26.5–19 ka, MIS 2), whereas other numerical dating techniques including radiocarbon, U-series, and OSL indicate



446 earlier local glacial maxima (80–30 ka, MIS 4 to MIS 3) in the Cantabrian Mountains, Pyrenees, Italian Apennines
447 and Pindus Mountains (e.g., Oliva et al., 2019; Jimenez-Sanchez et al., 2013). Another inter-range asynchrony was
448 observed in mountain glaciers of North America. They reached their maximum extent from as old as 25–24 ka for
449 some moraines and outwash in Sierra Nevada to as young as 17–15 ka for some terminal moraines in the Rocky
450 Mountains but a clear central tendency exists with a mean of ~19.5 ka (Laabs et al., 2020; Palacios et al., 2020; Young
451 et al., 2011). Relatively younger ages (HS-1) across the mountains located in the higher latitude were interpreted as a
452 sign of glacial post-LGM culmination in response to increased delivery of westerly derived moisture which reached
453 the northern continental interior of the western U.S after the large ice sheets started to retreat (Thackray, 2008,
454 Licciardi et al., 2004, Licciardi et al., 2001). For instance, younger exposure ages of last glacial maxima in the western
455 Uinta mountains, compared to mountain ranges farther east and north, reflected the influence of pluvial Lake
456 Bonneville after recession of Laurentide ice sheet to the north (Laabs et al., 2009).

457 Medium scale inter-range asynchrony (several thousand years) was observed in Yellowstone plateau.
458 Terminal moraines dated to ~17 ka are common in valleys along the north eastern mountains (e.g. Eightmile, Chico,
459 Pine Creek, S.Fork Deep Creek, Cascade Canyon and Gallatin) of the Great Yellowstone plateau. Glaciers in Teton
460 Range (south western part of the plateau) have terminal moraine with age of ~15 ka. Local LGM maxima dated to
461 ~19.8 to 18.2 ka in the western part of the plateau (Beartooth Uplift). Licciardi and Pierce (2018) suggested that
462 shifting orographic precipitation pattern due to formation of ice dome and change in ice flow direction caused
463 asynchrony in the Great Yellowstone region.

464 No or very small number of glacial chronologies document intra-range asynchrony for the latest glacial
465 termination. Age dating results from some relatively well-studied mountain ranges (Wasatch, Uinta, Bighorn ranges
466 in North America) present that intra-range asynchrony in glacial maxima in their various aspect (Laabs et al., 2020).
467 Some of them had LGM age ranging from hundreds to thousands of years from valley to valley. In the Wasatch range,
468 terminal moraines dated to ~21.9 ka (Laabs and Munroe, 2016), ~20.8 ka, 17.3 ka (Laabs et al., 2011) in three western
469 valleys, 19.6 ka in the southwestern valley and 17.6 ka, 17.3 ka in the southeastern valleys (Quirk et al., 2020).
470 Similarly, last glacial terminal moraine age difference of ~1 kyr observed between north-facing and south-facing slope,
471 Eastern Pyrenees (Delmas et al., 2011; Delmas et al., 2008). Even glaciers on the same oriented slope contain some
472 chronology difference. LGM moraine chronology from the three valleys on the east side of the central Sawatch range
473 varies from 22.3 ka to 19.9 ka (Young et al., 2011). Nevertheless, we suggest that some internal, external, analytical
474 uncertainties associated with sampling, measurements, or/and statistical approach can cause the low magnitude of
475 asynchrony in such small intra-range or massif. Some studies have attributed intra-range asynchrony in terminal
476 moraine ages to contrasting valley glacier response times related to topography, ice dynamics and/or differences in
477 glacier shape and hypsometry (Young et al., 2011, Licciardi and Pierce, 2018). As mentioned above, large and medium
478 scale asynchrony in the mountain glaciers across the North Atlantic region mostly explained by precipitation
479 distribution due to the relative location of the moisture source area and atmospheric circulation contributed by
480 topography. However intra-range or intra-massif scale of asynchrony in last glacial period needs further research to
481 be fully understood.

482



483 **6.3. Aspect effect on asynchronous maximum glacier extent**

484 Previous research indicates that the retreat or advance pattern of glaciers in some regions is not necessarily expected
485 to be uniform, coincidental, or synchronous with the primary factors (Fig. 8). Based on proxies from lacustrine (Orog)
486 sediment cores, the local LGM ranges between 19 and 18 ka near the Ih Bogd massif (Yu et al., 2017; Yu et al., 2019).
487 However, deglaciation started in Ih Artsan valley (south-facing) nearly a thousand years earlier (20.1 ± 0.7) than local
488 LGM. For the Jargalant valley (north-facing), we could not find the actual evidence of the latest deglaciation. If we
489 consider both glaciers moved synchronously, the geological evidence (terminal moraine) near 20 ka must have been
490 degraded by Bituut mainstream or/and reworked with the mass movement. Contrary, if the Jargalant glacier advanced
491 maximally near 17.2 ka based on exposure age dating, deglaciation must have begun 3000 years later in Jargalant
492 valley than in Ih Artsan valley. In this case, the most extensive glacial extent in Jargalant valley should represent LGM
493 glacial survival or significant glacial re-advance near 17 ka as the same as glacier advance in Mongolia and North
494 Atlantic region during HS-1.

495 In either case, changes in glacier mass balance in small massif or mountain (intra-range) could show large
496 spatial variation due to local topography-driven climatic factors: 1) snow avalanching, 2) preferential deposition of
497 wind-drifted snow (Florentine et al., 2020), 3) solar radiation, 4) temperature.

- 498 1. Periodically occurring snow avalanches support glacial accumulation. Most avalanches have steep slopes between
499 25° and 50° to slide down (Luckman, 1977). Both valleys are connected to the flat top and are less steep than the
500 threshold slope of 25° ; Jargalant valley is 23° for Jargalant and 18.2° for Ih Artsan. Very wet snow lubricated
501 with water can cause an avalanche on a slope of only 10 to 25° (Luckman, 1977). However, it is not significantly
502 relevant to our study area because Ih Bogd and its neighboring area experienced very cold and dry conditions
503 during MIS 2 (e.g., Yu et al., 2019).
- 504 2. Wind-drifted snow accumulation occurs either with or without snowfall. Wind deflates the snow from the
505 windward slope and redistributes it into the leeward slope. However, the prevailing wind direction of the study
506 area is northwest to southeast, which is the almost perpendicular direction to the orientations of the two valleys.
507 We assume the wind direction during MIS 2 was similar to the present with much strength. Therefore, wind
508 drifted snow may not significantly affect glacier accumulation. For that reason, we used the same precipitation
509 value in both valleys.
- 510 3. North-facing slopes in the northern hemisphere receive less solar radiation because of the aspect effect. Ih Bogd
511 locates in a mid-latitude great sunlight climate; furthermore, it has steeper relief which can enhance the aspect
512 effect. (Evans and Cox, 2005). Topographic shading can also influence glacier response and mass balance in
513 mountainous areas (Olson and Rupper, 2019). As expected, our modelling results demonstrate that the north-
514 facing slope receives less summer insolation than the south-facing slope, resulting in reduced glacial melt (5-10%)
515 under the same temperature conditions. Our 2D ice surface model suggests that an aspect affects the amount of
516 melt, however in a very small amount. This small reduction in the melt due to the shading effect could not stagnate
517 glaciers or cause significant glacier to advance for 3000 years. Under the same temperature, glaciers on the north
518 and south-facing slopes across small regions behave almost synchronously.



519 4. Some previous studies suggest that temperature is lower on the north-facing slopes at the same altitude. On the
520 north-facing slope of Taibai, Qinling mountains, JJA monthly mean temperature is measured 0.5–1 °C lower than
521 on the south-facing slope in the altitude range of 1250–3750 m (Tang & Fang, 2006). The vegetation distribution
522 on Mongolia's north-facing and south-facing slopes can prove the contrast in temperature and moisture on sunny
523 and shady slopes. In the field, we can easily see that trees grow only on the northern slope within the forest-step
524 zone in Mongolia (Fig. 7d, 7e). According to these facts, a small temperature difference is real and needs to be
525 considered. When we set the present-day temperature of Jargalant to 0.5 °C colder than in the Ih Artsan, 2D ice
526 surface modelling results perfectly match with the ¹⁰Be age dating results (Fig. 9). In this case, glaciers retreated
527 from their distal location asynchronously. The retreat of Ih Artsan glacier started near 20.23 ka (age dating result
528 was 20.1 ka), while Jargalant glacier started to retreat near 17.13 ka (age dating result was 17.2 ka). There were
529 small fluctuations in the ice advance and retreat with temperature changes in both cases, synchronous and
530 asynchronous.

531 In conclusion, glacier volume and area changes are likely to be sensitive to temperature change during cold
532 periods (22–16 ka) in semi-arid and arid regions, such as Ih Bogd (Batbaatar et al., 2018). Based on the age dating
533 and 2D ice surface modelling, we propose that the glaciers on the north- and south-facing slopes of Ih Bogd were able
534 to reach their maximum extent at different times with a 3 kyr temporal gap, caused by a combination of aspect-driven
535 melt rate and temperature difference.

536
537

538 **6.4. Morphostratigraphic mismatch in exposure age dating from erratic boulders, Jargalant valley**

539 **6.4.1. Inheritance from the summit plateau**

540 The massif has a steep slope; in particular, the slope reaches 32–70° along cirque walls and incised valleys .
541 Colluvial materials covering hillslopes and long boulder corridors were mainly the results of the active mass wasting
542 process. Particularly, rockfall deposits forming scree and talus apron must be the product of steep slope failure of the
543 summit plateau (Fig. 10). We expected that inner moraine crests would present Holocene or HS-1 exposure in light of
544 morphostratigraphy. M_{J2}, M_{J3}, and M_{J4} moraine crests have exposure ages ranging from 636.2 to 35.9 ka (Table 2, Fig.
545 5). According to moraine stratigraphy, exposure ages of inner moraines cannot be older than the age of the distal
546 moraine. The apparent ages show antiquity and scatter in its distribution, which cannot be a single geologic event;
547 associating the mean age with the specific timing of glacial termination is not appropriate (Heyman et al., 2011b). It
548 was more likely that the exposure ages from M_{J2}, M_{J3}, and M_{J4} moraines were due to the inherited ¹⁰Be concentration
549 produced during prior exposure in the boulders recycled from the cirque wall or paleo summit plateau by rockfall or
550 toppling during glaciation and/or paraglacial period. The shorter distance from the cirque wall was not enough for a
551 glacier to erode the rock surface, including inheritance during transportation to the final position (Fig. 11d-f). On the
552 other hand, this pattern would be contributed by enhanced rock-slope failure (de-buttressing) right after rapid
553 deglaciation (Hashemi et al., 2022; Ballantyne and Stone, 2012; Cossart et al., 2008).

554

555 **6.4.2. Cenozoic evolution of the low-lying, high-elevated summit plateau**



556 We recalculated the exposure age and erosion rate for the paleo-summit plateau using ^{10}Be concentrations
557 from those reworked boulders and production rate at the elevation of 3625 m which is the highest point between
558 Jargalant and Ih Artsan cirques (Fig. 11). Maximum exposure age of the flat summit plateau was calculated as 442.3
559 ± 29.8 ka, and the corresponding erosion rate of the summit plateau was 1.23 ± 0.10 m Myr $^{-1}$, which falls well into
560 the common denudation rate of arid region. (Table 2).

561 The flat summit plateau of the Ih Bogd massif is considered an uplifted paleo-peneplanation surface. The
562 basement structure of Ih Bogd was formed by the collision of the WNW-ESE to ENE-WSW oriented amalgamated
563 terranes throughout the Precambrian and Paleozoic (Şengör et al., 1993). $^{40}\text{Ar}/^{39}\text{Ar}$ ages from extrusive volcanic on
564 the Ih Bogd summit and apatite fission-track data show two significant uplifts that occurred in the Gobi-Altay range
565 and Ih Bogd history (Jolivet et al., 2007; Vassallo et al., 2007). The first uplift related to early to mid-Jurassic, the
566 region experienced crustal shortening events greater than 2 km. Gobi-Altay has been observed elsewhere in central
567 Asia through this event that is possibly due to a collision between Mongol-Okhotsk and Siberia or the Lhasa and
568 Qiangtang block to the far south in Tibet (Cunningham, 2010; Dewey et al., 1988; Traynor and Sladen, 1995). The
569 present erosional surface of the summit plateau formed just after this Jurassic exhumation and was preserved under a
570 negligible erosion rate. Preservation of this flat summit plateau and its fission-track age indicate quiescence without
571 significant vertical crustal motions continued until the last uplift began (Cunningham, 2010; Jolivet et al., 2007;
572 Vassallo et al., 2007).

573 The Gobi-Altay range is one of the northernmost far-fields affected by the Cenozoic tectonic collision of
574 India into Asia, which initiated the late Cenozoic reactivation and present-day stress regime (Cunningham et al., 1996;
575 Vassallo et al., 2007). According to the apatite fission track data of Vassallo et al. (2007), the onset of the last and
576 ongoing uplift corresponds to the late Cenozoic, 5 ± 3 Ma. This tectonic reactivation is responsible for creating the
577 high topography (~4000 m a.s.l) seen today, in the response to which faster exhumation is initiated as well (Vassallo
578 et al., 2007).

579 The paleo-erosion surfaces at high altitudes experienced rapid uplift after a long time of quiescence with low
580 erosion. Cosmogenic nuclides-based denudation rates from global paleo-erosion surfaces in diverse climatic, tectonic,
581 and lithologic environments do not exceed ~ 20 m Myr $^{-1}$ (Byun et al., 2015). We obtained erosion rate for flat summit
582 plateau using production rate at summit plateau and ^{10}Be concentrations of reworked boulders from M_{14} , M_{13} , and M_{12}
583 moraines. Calculated bedrock erosion rate for last ~ 600 ka for summit plateau ranged from 1.23 ± 0.10 m Myr $^{-1}$ to
584 25.8 ± 5.75 m Myr $^{-1}$. The erosion rate of 25.8 ± 5.75 m Myr $^{-1}$ was thought to be a maximum value because erosion
585 probably increases with the increasing elevation of the uplifting massif. This result was harmonious with the long-
586 term (since the last uplift) exhumation rate of 23.6 ± 3 m Ma $^{-1}$ (Vassallo et al., 2011) and Holocene erosion rate of 28
587 m Myr $^{-1}$ (Jolivet et al., 2007) for the massif. Whereas flatness and the lowest erosion rate of 1.23 ± 0.10 m Myr $^{-1}$ reveal
588 negligible erosion and notable preservation of paleo-surface for several hundred thousand years. If this erosion rate
589 reflects an average rate that can be applied to the entire flat surface and has been maintained for the total uplift period
590 of the massif (Vassallo et al., 2007), it would account for only the 2 to 7.6 m of erosion.



591 **7. CONCLUSIONS**

592 Central Asian valley glaciers, including Ih Bogd massif, expanded and shrank, presenting more complex behavior
593 relative to large ice sheets in the northern hemisphere. Regional climate and local non-climatic factors have been
594 playing an essential role in this complexity. Our ^{10}Be dating documents that the maximum advance in Ih Artsan valley
595 on the southern slope occurred at 20.1 ka (M_{Ih1}), generally falling within the gLGM, whereas large terminal moraine
596 formed around 17.2 ka (M_{J1}) in the Jargalant valley on the northern slope.

597 Asynchrony in glacier expansion has been reported from some of areas in the globe but has not been clearly
598 studied with a combination of geochronologic and numerical modeling approaches. The glacier chronology itself
599 provides the possibility of both explanations, synchronous and asynchronous expansion of glacier. Glaciers of Ih
600 Artsan and Jargalant valleys advanced and retreated synchronously in the same LGM summer temperature. Due to
601 aspect-driven solar insolation change, paleoglacier in the north-facing Jargalant valley melted slower (5-10%) than
602 the glacier in Ih Artsan valley. However, this amount of melt difference could not produce glacier advance or
603 stagnation for a long period. Asynchronous glaciation was observed across the study area if the LGM summer
604 temperature in Jargalant valley was 0.5 °C lower than in Ih Artsan due to aspect-driven temperature change. According
605 to the lower temperature case, Jargalant glacier retreated from the most extensive position 3000 years later than Ih
606 Artsan glacier. The temperature difference driven by aspect on both slopes significantly affects the glaciers to survive
607 longer than when the aspect-driven insolation only affects the glacier melt.

608 The glacial retreat began soon after the peak of local glacial maximum on both valleys and left several
609 sequences of inner moraines in their heads (cirques). Inner moraine at the south-facing cirque dated to ~ 13.5 ka
610 (Batbaatar et al., 2018), however on the north-facing cirque, transported boulders show a significantly old exposure
611 age (636.2 to 35.9 ka) for inner moraines (M_{J2} - M_{J4}). The summit plateau of the Ih Bogd massif is one of the oldest
612 known tectonically uplifted surfaces on Earth. It is more likely that extremely old exposure ages are the result of
613 inheritance recycled from rock falls from the paleo-erosional surface of the summit plateau.



614 *Data availability.* The data that supports the findings of this study are available within the article [and its
615 supplementary material]

616

617 *Author contributions.* YBS planned the study and proceeded a field investigation with JSO, PK, KS, and CHL. YBS
618 designed a funding acquisition. JSO designed ^{10}Be lab experiments with RHH and BYY. CHL and MKS developed
619 a matlab code of the 2D ice surface modelling and performed the simulation. PK and YBS prepared the manuscript
620 with contributions from all co-authors.

621

622 *Competing interests.* The contact author has declared that neither they nor their co-authors have any competing
623 interests.

624

625 *Disclaimer.* Publisher's note: Copernicus Publications remains neutral with regard to jurisdictional claims in
626 published maps and institutional affiliations.

627

628 *Acknowledgments.* This work was supported by the Ministry of Education of the Republic of Korea and the National
629 Research Foundation of Korea (NRF-2018S1A5A2A01031348 for Y.B.S).

630



631 **REFERENCES**

- 632 ©JAXA/METI., 2007. ALOS PALSAR L1.0 High-resolution terrain corrected dataset. Accessed through ASF DAAC,
633 <https://asf.alaska.edu>, 25 June 2009. <https://doi.org/10.5067/J4JVCFDDPEW1>
- 634 An, Z., Kukla, G., Porter, S.C., Xiao, J.: Late Quaternary dust flow on the Chinese loess plateau, *Catena*, 18(2), 125-
635 132, [https://doi.org/10.1016/0341-8162\(91\)90012-M](https://doi.org/10.1016/0341-8162(91)90012-M), 1991.
- 636 Balco, G., Stone, J.O., Lifton, N.A., Dunai, T.J.: A complete and easily accessible means of calculating surface
637 exposure ages or erosion rates from ^{10}Be and ^{26}Al measurements, *Quat. Geochronol.*, 3(3), 174-195,
638 <https://doi.org/10.1016/j.quageo.2007.12.001>, 2008.
- 639 Ballantyne, C.K., Stone, J.O.: Timing and periodicity of paraglacial rock-slope failures in the Scottish Highlands,
640 *Geomorphology*, 186, 150-161, <https://doi.org/10.1016/j.geomorph.2012.12.030>, 2013.
- 641 Barr, I.D., Lovell, H.: A review of topographic controls on moraine distribution, *Geomorphology*, 226, 44-64,
642 <https://doi.org/10.1016/j.geomorph.2014.07.030>, 2014.
- 643 Batbaatar, J., Gillespie, A.R.: Outburst floods of the Maly Yenisei. Part II—new age constraints from Darhad basin,
644 *Int. Geol. Rev.*, 58(14), 1753-1779, <https://doi.org/10.1080/00206814.2016.1193452>, 2016.
- 645 Batbaatar, J., Gillespie, A.R., Fink, D., Matmon, A., Fujioka, T.: Asynchronous glaciations in arid continental climate,
646 *Quat. Sci. Rev.*, 182, 1-19, <https://doi.org/10.1016/j.quascirev.2017.12.001>, 2018.
- 647 Bayasgalan, A., Jackson, J., Ritz, J.F., Carretier, S.J.T.: Field examples of strike-slip fault terminations in Mongolia
648 and their tectonic significance. *Tectonics*, 18(3), 394-411, <https://doi.org/10.1029/1999TC900007>, 1999.
- 649 Benn, D. I., and Hulton, N. R.: An Excel™ spreadsheet program for reconstructing the surface profile of former
650 mountain glaciers and ice caps, *Comput. Geosci*, v. 36, no. 5, p. 605-610,
651 <https://doi.org/10.1016/j.cageo.2009.09.016>, 2010,
- 652 Benn, D.I., Lehmkuhl, F.: Mass balance and equilibrium-line altitudes of glaciers in high-mountain environments,
653 *Quat. Int.*, 65(Supplement C), 15-29, [https://doi.org/10.1016/S1040-6182\(99\)00034-8](https://doi.org/10.1016/S1040-6182(99)00034-8), 2000.
- 654 Berger, A., and Loutre, M.-F.: Insolation values for the climate of the last 10 million years, *Quat. Sci. Rev.*, v. 10, no.
655 4, p. 297-317, [https://doi.org/10.1016/0277-3791\(91\)90033-Q](https://doi.org/10.1016/0277-3791(91)90033-Q), 1991,
- 656 Berkey, C.P., Morris, F.K.: The peneplanes of Mongolia, *Am. Mus. Novit.*, 136, 1-11, 1924.
- 657 Blomdin, R., Stroeven, A.P., Harbor, J.M., Gribenski, N., Caffee, M.W., Heyman, J., Rogozhina, I., Ivanov, M.N.,
658 Petrakov, D.A., Walther, M.: Timing and dynamics of glaciation in the Ikh Turgan Mountains, Altai region,
659 High Asia, *Quat. Geochronol.*, 47, 54-71, <https://doi.org/10.1016/j.quageo.2018.05.008>, 2018.
- 660 Blomdin, R., Stroeven, A.P., Harbor, J.M., Lifton, N.A., Heyman, J., Gribenski, N., Petrakov, D.A., Caffee, M.W.,
661 Ivanov, M.N., Hättestrand, C., Rogozhina, I., Usabaliyev, R.: Evaluating the timing of former glacier
662 expansions in the Tian Shan: A key step towards robust spatial correlations, *Quat. Sci. Rev.*, 153, 78-96,
663 <https://doi.org/10.1016/j.quascirev.2016.07.029>, 2016.
- 664 Buizert, C., Keisling, B., Box, J., He, F., Carlson, A., Sinclair, G., and DeConto, R.: Greenland-wide seasonal
665 temperatures during the last deglaciation, *Geophys. Res. Lett.*, v. 45, no. 4, p. 1905-1914,
666 <https://doi.org/10.1002/2017GL075601>, 2018,



- 667 Byun, J., Heimsath, A.M., Seong, Y.B., Lee, S.Y.: Erosion of a high-altitude, low-relief area on the Korean Peninsula:
668 implications for its development processes and evolution, *Earth Surf. Process. Landf.*, 40(13), 1730-1745,
669 <https://doi.org/10.1002/esp.3749>, 2015.
- 670 Chauvenet, W.: *A Manual of spherical and practical astronomy*-Vol. 1: Spherical astronomy; Vol. 2: Theory and use
671 of astronomical instruments. Method of least squares, 5th ed., revised and corr, Dover Publication, New York,
672 1960
- 673 Chen, Y., Li, Y., Wang, Y., Zhang, M., Cui, Z., Yi, C., Liu, G.: Late Quaternary glacial history of the Karlik Range,
674 easternmost Tian Shan, derived from ¹⁰Be surface exposure and optically stimulated luminescence datings,
675 *Quat. Sci. Rev.*, 115, 17-27, <https://doi.org/10.1016/j.quascirev.2015.02.010>, 2015.
- 676 Ciner, A., Sarikaya, M. A., Yildirim, C.: Misleading old age on a young landform? The dilemma of cosmogenic
677 inheritance in surface exposure dating: Moraines vs. rock glaciers, *Quat. Geochronol.*, 42, 76-88,
678 <https://doi.org/10.1016/j.quageo.2017.07.003>, 2017.
- 679 Clark, P.U., Dyke, A.S., Shakun, J.D., Carlson, A.E., Clark, J., Wohlfarth, B., Mitrovica, J.X., Hostetler, S.W.,
680 McCabe, A.M.: The last glacial maximum, *Science*, 325(5941), 710-714,
681 <https://doi.org/10.1126/science.1172873>, 2009.
- 682 Cossart, E., Braucher, R., Fort, M., Bourlès, D., Carcaillet, J.: Slope instability in relation to glacial debuttressing in
683 alpine areas (Upper Durance catchment, southeastern France): evidence from field data and ¹⁰Be cosmic ray
684 exposure ages, *Geomorphology*, 95(1-2), 3-26, <https://doi.org/10.1016/j.geomorph.2006.12.022>, 2008.
- 685 Cunningham, D.: Tectonic setting and structural evolution of the Late Cenozoic Gobi Altai orogen, *J. Geol. Soc.*
686 *London.*, 338(1), 361-387, <https://doi.org/10.1144/SP338.17>, 2010.
- 687 Cunningham, W.D., Windley, B.F., Dorjnamjaa, D., Badamgarov, J., Saandar, M.: Late Cenozoic transpression in
688 southwestern Mongolia and the Gobi Altai-Tien Shan connection, *Earth Planet. Sci. Lett.*, 140(1-4), 67-81,
689 [https://doi.org/10.1016/0012-821X\(96\)00048-9](https://doi.org/10.1016/0012-821X(96)00048-9), 1996.
- 690 Delmas, M., Calvet, M., Gunnell, Y., Braucher, R., & Bourlès, D.: Palaeogeography and ¹⁰Be exposure-age
691 chronology of Middle and Late Pleistocene glacier systems in the northern Pyrenees: implications for
692 reconstructing regional palaeoclimates, *Palaeogeog. Palaeoclimatol. Palaeoecol.*, 305(1-4), 109-122,
693 <https://doi.org/10.1016/j.palaeo.2011.02.025>, 2011.
- 694 Delmas, M., Gunnell, Y., Braucher, R., Calvet, M., & Bourlès, D.: Exposure age chronology of the last glaciation in
695 the eastern Pyrenees, *Quat. Res.*, 69(2), 231-241, <https://doi.org/10.1016/j.yqres.2007.11.004>, 2008.
- 696 Devyatkin, E.: Structures and formational complexes of the Cenozoic activated stage. *Tectonics of the Mongolian*
697 *People's Republic*, Nauka, 41, 182-195, 1974.
- 698 Dewey, J.F., Shackleton, R.M., Chengfa, C., Yiyin, S.: The tectonic evolution of the Tibetan Plateau, *Philos. Trans.*
699 *Royal Soc. A.*, 327(1594), 379-413, <https://doi.org/10.1098/rsta.1988.0135>, 1988.
- 700 Evans, I.S., Cox, N.J.: Global variations of local asymmetry in glacier altitude: separation of north-south and east-
701 west components, *J. Glaciol.*, 51(174), 469-482, <https://doi.org/10.3189/172756505781829205>, 2005.



- 702 Farr, T.G., Rosen, P.A., Caro, E., Crippen, R., Duren, R., Hensley, S., Kobrick, M., Paller, M., Rodriguez, E., Roth,
703 L.: The shuttle radar topography mission, *Rev. Geophys.*, 45(2) DOI:
704 <https://doi.org/10.1029/2005RG000183>, 2007.
- 705 Felauer, T., Schlütz, F., Murad, W., Mischke, S., Lehmkuhl, F.: Late Quaternary climate and landscape evolution in
706 arid Central Asia: A multiproxy study of lake archive Bayan Tohomin Nuur, Gobi desert, southern Mongolia,
707 *J. Asian. Earth. Sci.*, 48, 125-135, <https://doi.org/10.1016/j.jseas.2011.12.002>, 2012.
- 708 Fletcher, W.J., Goni, M.F.S., Allen, J.R., Cheddadi, R., Combourieu-Nebout, N., Huntley, B., Lawson, I., Londeix,
709 L., Magri, D., Margari, V.: Millennial-scale variability during the last glacial in vegetation records from
710 Europe, *Quat. Sci. Rev.*, 29(21-22), 2839-2864, <https://doi.org/10.1016/j.quascirev.2009.11.015>, 2010.
- 711 Florentine, C., Harper, J., Fagre, D.: Parsing complex terrain controls on mountain glacier response to climate forcing,
712 *Glob. Planet. Change.*, 191, 103209, <https://doi.org/10.1016/j.gloplacha.2020.103209>, 2020.
- 713 Garnier, B., and Ohmura, A.: A method of calculating the direct shortwave radiation income of slopes, *J. Appl.*
714 *Meteorol. Climatol.*, v. 7, no. 5, p. 796-800, [https://doi.org/10.1175/1520-0450\(1968\)007<0796:AMOCTD>2.0.CO;2](https://doi.org/10.1175/1520-0450(1968)007<0796:AMOCTD>2.0.CO;2), 1968.
- 716 Gillespie, A., Molnar, P.: Asynchronous maximum advances of mountain and continental glaciers, *Rev. Geophys.*,
717 33(3), 311-364, <https://doi.org/10.1029/95RG00995>, 1995.
- 718 Gillespie, A.R., Burke, R.M., Komatsu, G., Bayasgalan, A.: Late Pleistocene glaciers in Darhad basin, northern
719 Mongolia, *Quat. Res.*, 69(2), 169-187, <https://doi.org/10.1016/j.yqres.2008.01.001>, 2008.
- 720 Goldthwait, R.P.: Mountain glaciers of the Presidential Range in New Hampshire, *Arc. Alp. Res.*, 2(2), 85-102,
721 <https://doi.org/10.1080/00040851.1970.12003566>, 1970.
- 722 Gosse, J.C., Phillips, F.M.: Terrestrial in situ cosmogenic nuclides: theory and application, *Quat. Sci. Rev.*, 20(14),
723 1475-1560, [https://doi.org/10.1016/S0277-3791\(00\)00171-2](https://doi.org/10.1016/S0277-3791(00)00171-2), 2001.
- 724 Hashemi, K., Sarıkaya, M.A., Görüm, T., Wilcken, K.M., Çiner, A., Žebre, M., Stepišnik, U., Yıldırım, C.: The
725 Namaras rock avalanche: Evidence of mid-to-late Holocene paraglacial activity in the Central Taurus
726 Mountains, SW Turkey, *Geomorphology*, 408, 108261, <https://doi.org/10.1016/j.geomorph.2022.108261>,
727 2022.
- 728 Heyman, J.: Paleoglaciation of the Tibetan Plateau and surrounding mountains based on exposure ages and ELA
729 depression estimates, *Quat. Sci. Rev.*, 91, 30-41, <https://doi.org/10.1016/j.quascirev.2014.03.018>, 2014.
- 730 Heyman, J., Stroeven, A.P., Caffee, M.W., Hättestrand, C., Harbor, J.M., Li, Y., Alexanderson, H., Zhou, L., Hubbard,
731 A.: Palaeoglaciology of Bayan Har Shan, NE Tibetan Plateau: exposure ages reveal a missing LGM
732 expansion, *Quat. Sci. Rev.*, 30(15-16), 1988-2001, <https://doi.org/10.1016/j.quascirev.2011.05.002>, 2011a.
- 733 Heyman, J., Stroeven, A.P., Harbor, J.M., Caffee, M.W.: Too young or too old: evaluating cosmogenic exposure
734 dating based on an analysis of compiled boulder exposure ages, *Earth Planet. Sci. Lett.*, 302(1-2), 71-80,
735 <https://doi.org/10.1016/j.epsl.2010.11.040>, 2011b.
- 736 Hock, R.: Modelling of glacier melt and discharge: ETH Zurich-, 1999, A distributed temperature-index ice-and
737 snowmelt model including potential direct solar radiation, *J. Glaciol.*, v. 45, no. 149, p. 101-111,
738 <https://doi.org/10.3189/S0022143000003087>, 1998,



- 739 Hock, R.: A distributed temperature-index ice-and snowmelt model including potential direct solar radiation, *J.*
740 *Glaciol.*, 45(149), 101-111, <https://doi.org/10.3189/S0022143000003087>, 1999.
- 741 Hughes, P.D., Gibbard, P.L., Ehlers, J.: Timing of glaciation during the last glacial cycle: evaluating the concept of a
742 global ‘Last Glacial Maximum’(LGM). *Earth-Sci. Rev.*, 125, 171-198,
743 <https://doi.org/10.1016/j.earscirev.2013.07.003>, 2013.
- 744 Iqbal, M.: *An Introduction to Solar Radiation*, New York, Academic Press, 1983
- 745 Jiménez-Sánchez, Montserrat, et al.: "A review of glacial geomorphology and chronology in northern Spain: timing
746 and regional variability during the last glacial cycle.", *Geomorphology*, 196, 50-64,
747 <https://doi.org/10.1016/j.geomorph.2012.06.009>, 2013.
- 748 Jolivet, M., Ritz, J.-F., Vassallo, R., Larroque, C., Braucher, R., Todbileg, M., Chauvet, A., Sue, C., Arnaud, N., De
749 Vicente, R.: Mongolian summits: an uplifted, flat, old but still preserved erosion surface, *Geology*, 35(10),
750 871-874, <https://doi.org/10.1130/G23758A.1>, 2007.
- 751 Jones, R., Small, D., Cahill, N., Bentley, M., Whitehouse, P.: iceTEA: tools for plotting and analysing cosmogenic-
752 nuclide surface-exposure data from former ice margins, *Quat. Geochronol.*, 51, 72-86,
753 <https://doi.org/10.1016/j.quageo.2019.01.001>, 2019.
- 754 Jouzel, J., Stievenard, M., Johnsen, S.J., Landais, A., Masson-Delmotte, V., Sveinbjornsdottir, A., Vimeux, F., Von
755 Grafenstein, U., White, J.W.: The GRIP deuterium-excess record, *Quat. Sci. Rev.*, 26(1-2), 1-17,
756 <https://doi.org/10.1016/j.quascirev.2006.07.015>, 2007.
- 757 Karger, D.N., Conrad, O., Böhner, J., Kawohl, T., Kreft, H., Soria-Auza, R.W., Zimmermann, N.E., Linder, H.P.,
758 Kessler, M.: Climatologies at high resolution for the earth’s land surface areas. *Sci. Data.*, 4, 170122,
759 <https://doi.org/10.1038/sdata.2017.122>, 2017.
- 760 Khandsuren, P., Seong, Y.B., Oh, J.S., Rhee, H.H., Sandag, K., Yu, B.Y.: Late Quaternary glacial history of Khentey
761 Mountains, Central Mongolia, *Boreas*, 48(3), 779-799, doi.org/10.1111/bor.12386, 2019.
- 762 Kirkbride, M., Winkler, S.: Correlation of Late Quaternary moraines: impact of climate variability, glacier response,
763 and chronological resolution, *Quat. Sci. Rev.*, 46, 1-29, <https://doi.org/10.1016/j.quascirev.2012.04.002>,
764 2012.
- 765 Klinge, M., Böhner, J., Lehmkuhl, F.: Climate Pattern, Snow-and Timberlines in the Altai Mountains, Central Asia
766 (Klimaverhältnisse, Schnee-und Waldgrenzen im Altai Gebirge, Zentralasien), *Erdkunde*, 296-308, 2003.
- 767 Kohl, C.P., Nishiizumi, K.: Chemical isolation of quartz for measurement of in situ -produced cosmogenic nuclides,
768 *Geochim. Cosmochim. Acta*, 56(9), 3583-3587, [https://doi.org/10.1016/0016-7037\(92\)90401-4](https://doi.org/10.1016/0016-7037(92)90401-4), 1992.
- 769 Koppes, M., Gillespie, A.R., Burke, R.M., Thompson, S.C., Stone, J.: Late quaternary glaciation in the Kyrgyz Tien
770 Shan. *Quat. Sci. Rev.*, 27(7-8), 846-866, <https://doi.org/10.1016/j.quascirev.2008.01.009>, 2008.
- 771 Laabs, B. J., Licciardi, J. M., Leonard, E. M., Munroe, J. S., & Marchetti, D. W.: Updated cosmogenic chronologies
772 of Pleistocene mountain glaciation in the western United States and associated paleoclimate inferences, *Quat.*
773 *Sci. Rev.*, 242, 106427, <https://doi.org/10.1016/j.quascirev.2020.106427>, 2020.
- 774 Laabs, B. J. C., & Munroe, J. S.: Late Pleistocene mountain glaciation in the Lake Bonneville basin, In *Developments*
775 *in Earth. Surf. Process.*, Vol. 20, pp. 462-503, <https://doi.org/10.1016/B978-0-444-63590-7.00017-2>, 2016



- 776 Laabs, B. J., Refsnider, K. A., Munroe, J. S., Mickelson, D. M., Applegate, P. J., Singer, B. S., & Caffee, M. W.:
777 Latest Pleistocene glacial chronology of the Uinta Mountains: support for moisture-driven asynchrony of the
778 last deglaciation, *Quat. Sci. Rev.*, 28(13-14), 1171-1187, <https://doi.org/10.1016/j.quascirev.2008.12.012>, 2009
- 779 Lal, D.: Cosmic ray labeling of erosion surfaces: in situ nuclide production rates and erosion models, *Earth Planet.*
780 *Sci. Lett.*, 104(2), 424-439, [https://doi.org/10.1016/0012-821X\(91\)90220-C](https://doi.org/10.1016/0012-821X(91)90220-C), 1991.
- 781 Lee, M.K., Lee, Y.I., Lim, H.S., Lee, J.I., Yoon, H.I.: Late Pleistocene–Holocene records from Lake Ulaan, southern
782 Mongolia: implications for east Asian palaeomonsoonal climate changes, *J. Quat. Sci.*, 28(4), 370-378,
783 <https://doi.org/10.1002/jqs.2626>, 2013.
- 784 Lehmkühl, F., Grunert, J., Hülle, D., Batkhisig, O., Stauch, G.: Paleolakes in the Gobi region of southern Mongolia,
785 *Quat. Sci. Rev.*, 179, 1-23, <https://doi.org/10.1016/j.quascirev.2017.10.035>, 2018.
- 786 Li, Y., Liu, G., Chen, Y., Li, Y., Harbor, J., Stroeven, A.P., Caffee, M., Zhang, M., Li, C., Cui, Z.: Timing and extent
787 of Quaternary glaciations in the Tianger Range, eastern Tian Shan, China, investigated using ¹⁰Be surface
788 exposure dating, *Quat. Sci. Rev.*, 98, 7-23, <https://doi.org/10.1016/j.quascirev.2014.05.009>, 2014.
- 789 Licciardi, J. M., Clark, P. U., Brook, E. J., Elmore, D., & Sharma, P.: Variable responses of western US glaciers during
790 the last deglaciation, *Geology*, 32(1), 81-84, <https://doi.org/10.1130/G19868.1>, 2004
- 791 Licciardi, J. M., Clark, P. U., Brook, E. J., Pierce, K. L., Kurz, M. D., Elmore, D., & Sharma, P.: Cosmogenic ³He
792 and ¹⁰Be chronologies of the late Pinedale northern Yellowstone ice cap, Montana, USA, *Geology*, 29(12),
793 1095-1098, [https://doi.org/10.1130/0091-7613\(2001\)029<1095:CHABCO>2.0.CO;2](https://doi.org/10.1130/0091-7613(2001)029<1095:CHABCO>2.0.CO;2), 2001.
- 794 Licciardi, J. M., & Pierce, K. L.: History and dynamics of the Greater Yellowstone Glacial System during the last two
795 glaciations, *Quat. Sci. Rev.*, 200, 1-33, <https://doi.org/10.1016/j.quascirev.2018.08.027>, 2018
- 796 Lifton, N., Sato, T., Dunai, T.J.: Scaling in situ cosmogenic nuclide production rates using analytical approximations
797 to atmospheric cosmic-ray fluxes, *Earth Planet. Sci. Lett.*, 386, 149-160,
798 <https://doi.org/10.1016/j.epsl.2013.10.052>, 2014.
- 799 Luckman, B. H.: The Geomorphic Activity of Snow Avalanches. *Geografiska Annaler: Series A, Phys. Geogr.*,
800 59(1-2), 31-48, <https://doi.org/10.1080/04353676.1977.11879945>, 1977.
- 801 Mischke, S., Lee, M.K., Lee, Y.I.: Climate history of southern Mongolia since 17 ka: The ostracod, gastropod and
802 charophyte record from Lake Ulaan, *Front. Earth Sci.*, 8, 221, <https://doi.org/10.3389/feart.2020.00221>,
803 2020.
- 804 NAGC, N.A.f.G.a.C., 1969. Topographic map of Mongolia Administration of Land Affairs of Mongolia, Ulaanbaatar,
805 Mongolia.
- 806 NAMEM, N.A.f.M.a.E.m., 2020. Climate data. Mongolian Statistical Information Service, Ulaanbaatar, Mongolia.
- 807 Nishiizumi, K., Imamura, M., Caffee, M., Southon, J., Finkel, R., McAninch, J.: Absolute calibration of ¹⁰Be AMS
808 Standards, *Nucl. Instrum. Methods Phys. Res. B.*, 258(2), 403-413,
809 <https://doi.org/10.1016/j.nimb.2007.01.297>, 2007.
- 810 National Oceanic and Atmospheric Administration.: US standard atmosphere (Vol. 76)., 1976



- 811 Oliva, M., Palacios, D., Fernández-Fernández, J. M., Rodríguez-Rodríguez, L., García-Ruiz, J. M., Andrés, N., ... &
812 Hughes, P. D.: Late Quaternary glacial phases in the Iberian Peninsula, *Earth-Sci. Rev.*, 192, 564-600,
813 <https://doi.org/10.1016/j.earscirev.2019.03.015>, 2019.
- 814 Olson, M., & Rupper, S.: Impacts of topographic shading on direct solar radiation for valley glaciers in complex
815 topography, *The Cryosphere*, 13(1), 29-40, 2019.
- 816 Palacios, D., Stokes, C. R., Phillips, F. M., Clague, J. J., Alcalá-Reygosa, J., Andrés, N., ... & Ward, D. J.: The
817 deglaciation of the Americas during the Last Glacial Termination, *Earth-Sci. Rev.*, 203, 103113,
818 <https://doi.org/10.1016/j.earscirev.2020.103113>, 2020.
- 819 Pötsch, S.: Dynamics and paleo-climatic forcing of late Pleistocene glaciers in the Turgen and Khangai mountains
820 (Mongolia) reconstructed from geomorphology, ¹⁰Be surface exposure dating, and ice flow modelling. Ph.D.
821 thesis, Greifswald, Finsterwalde, 2017.
- 822 Quirk, B. J., Moore, J. R., Laabs, B. J., Plummer, M. A., & Caffee, M. W.: Latest Pleistocene glacial and climate
823 history of the Wasatch Range, Utah, *Quat. Sci. Rev.*, 238, 106313,
824 <https://doi.org/10.1016/j.quascirev.2020.106313>, 2020.
- 825 Ross, S.M.: Peirce's criterion for the elimination of suspect experimental data, *J. Eng. Technol.*, 20(2), 38-41, 2003.
- 826 Rother, H., Lehmkuhl, F., Fink, D., Nottebaum, V.: Surface exposure dating reveals MIS-3 glacial maximum in the
827 Khangai Mountains of Mongolia, *Quat. Res.*, 82(2), 297-308, <https://doi.org/10.1016/j.yqres.2014.04.006>,
828 2014.
- 829 Roy, D.P., Wulder, M.A., Loveland, T.R., Woodcock, C., Allen, R.G., Anderson, M.C., Helder, D., Irons, J.R.,
830 Johnson, D.M., Kennedy, R.: Landsat-8: Science and product vision for terrestrial global change
831 research, *Remote. Sens. Environ.*, 145, 154-172, 2014.
- 832 Sahsamanoglou, H., Makrogiannis, T., Kallimopoulos, P.: Some aspects of the basic characteristics of the Siberian
833 anticyclone, *Int. J. Climatol.*, 11(8), 827-839, <https://doi.org/10.1002/joc.3370110803>, 1991.
- 834 Şengör, A., Natal'in, B., Burtman, V.: Evolution of the Altaid tectonic collage and Palaeozoic crustal growth in Eurasia,
835 *Nature*, 364(6435), 299-307, <https://doi.org/10.1038/364299a0>, 1993.
- 836 Seong, Y.B., Dorn, R.I., Yu, B.Y.: Evaluating the life expectancy of a desert pavement, *Earth-Sci.Rev.*, 162, 129-154,
837 <https://doi.org/10.1016/j.earscirev.2016.08.005>, 2016.
- 838 Shackleton, N.: Oxygen isotope analyses and Pleistocene temperatures re-assessed, *Nature*, 215(5096), 15-17,
839 <https://doi.org/10.1038/215015a0>, 1967.
- 840 Shackleton, N.J.: The 100,000-year ice-age cycle identified and found to lag temperature, carbon dioxide, and orbital
841 eccentricity, *Science*, 289(5486), 1897-1902, <https://doi.org/10.1126/science.289.5486.1897>, 2000.
- 842 Skinner, L., Shackleton, N.: An Atlantic lead over Pacific deep-water change across Termination I: implications for
843 the application of the marine isotope stage stratigraphy, *Quat. Sci. Rev.*, 24(5-6), 571-580,
844 <https://doi.org/10.1016/j.quascirev.2004.11.008>, 2005.
- 845 Smith, S.G., Wegmann, K.W., Ancuta, L.D., Gosse, J.C., Hopkins, C.E.: Paleotopography and erosion rates in the
846 central Hangay Dome, Mongolia: Landscape evolution since the mid-Miocene, *J. Asian. Earth. Sci.*, 125, 37-
847 57 DOI: <https://doi.org/10.1016/j.jseaes.2016.05.013>, 2016.



- 848 Stone, J.O.: Air pressure and cosmogenic isotope production, *J. Geophys. Res. Solid Earth.*, 105(B10), 23753-23759,
849 <https://doi.org/10.1029/2000JB900181>, 2000.
- 850 Tang, Z., & Fang, J.: Temperature variation along the northern and southern slopes of Mt. Taibai, China, *Agric. For.*
851 *Meteorol.*, 139(3-4), 200-207, <https://doi.org/10.1016/j.agrformet.2006.07.001>, 2006.
- 852 Tarasov, P., Peyron, O., Guiot, J., Brewer, S., Volkova, V., Bezusko, L., Dorofeyuk, N., Kvavadze, E., Osipova, I.,
853 and Panova, N.: Last Glacial Maximum climate of the former Soviet Union and Mongolia reconstructed from
854 pollen and plant macrofossil data, *Clim. Dyn.*, v. 15, no. 3, p. 227-240,
855 <https://doi.org/10.1007/s003820050278>, 1999.
- 856 Thackray, G. D.: Varied climatic and topographic influences on Late Pleistocene mountain glaciation in the western
857 United States, *J. Quat. Sci.*: Published for the Quaternary Research Association, 23(6-7), 671-681,
858 <https://doi.org/10.1002/jqs.1210>, 2008.
- 859 Thompson, W.G., Spiegelman, M.W., Goldstein, S.L., Speed, R.C.: An open-system model for U-series age
860 determinations of fossil corals, *Earth Planet. Sci. Lett.*, 210(1-2), 365-381, [https://doi.org/10.1016/S0012-821X\(03\)00121-3](https://doi.org/10.1016/S0012-821X(03)00121-3), 2003.
- 862 Tomurtogoo, O.: Geological map of Mongolia, 2014.
- 863 Traynor, J., Sladen, C.: Tectonic and stratigraphic evolution of the Mongolian People's Republic and its influence on
864 hydrocarbon geology and potential, *Mar. Pet. Geol.*, 12(1), 35-52, [https://doi.org/10.1016/0264-8172\(95\)90386-X](https://doi.org/10.1016/0264-8172(95)90386-X), 1995.
- 866 Vassallo, R., Jolivet, M., Ritz, J.-F., Braucher, R., Larroque, C., Sue, C., Todbileg, M., Javkhlanbold, D.: Uplift age
867 and rates of the Gurvan Bogd system (Gobi-Altay) by apatite fission track analysis, *Earth Planet. Sci. Lett.*,
868 259(3-4), 333-346, <https://doi.org/10.1016/j.epsl.2007.04.047>, 2007.
- 869 Vassallo, R., Ritz, J.-F., Carretier, S.: Control of geomorphic processes on ¹⁰Be concentrations in individual clasts:
870 Complexity of the exposure history in Gobi-Altay range (Mongolia), *Geomorphology*, 135(1-2), 35-47,
871 <https://doi.org/10.1016/j.geomorph.2011.07.023>, 2011.
- 872 Wang, Y.-J., Cheng, H., Edwards, R.L., An, Z., Wu, J., Shen, C.-C., Dorale, J.A.: A high-resolution absolute-dated
873 late Pleistocene monsoon record from Hulu Cave, China, *Science*, 294(5550), 2345-2348,
874 <https://doi.org/10.1126/science.1064618>, 2001.
- 875 Young, N. E., Briner, J. P., Leonard, E. M., Licciardi, J. M., & Lee, K.: Assessing climatic and nonclimatic forcing
876 of Pinedale glaciation and deglaciation in the western United States, *Geology*, 39(2), 171-174,
877 <https://doi.org/10.1130/G31527.1>, 2011.
- 878 Yu, K., Lehmkuhl, F., Diekmann, B., Zeeden, C., Nottebaum, V., Stauch, G.: Geochemical imprints of coupled
879 paleoenvironmental and provenance change in the lacustrine sequence of Orog Nuur, Gobi Desert of
880 Mongolia, *J. Paleolimnol.*, 58(4), 511-532, <https://doi.org/10.1007/s10933-017-0007-7>, 2017.
- 881 Yu, K., Lehmkuhl, F., Schlütz, F., Diekmann, B., Mischke, S., Grunert, J., Murad, W., Nottebaum, V., Stauch, G.,
882 Zeeden, C.: Late Quaternary environments in the Gobi Desert of Mongolia: Vegetation, hydrological, and
883 palaeoclimate evolution, *Palaeogeogr. Palaeoclimatol. Palaeoecol.*, 514, 77-91,
884 <https://doi.org/10.1016/j.palaeo.2018.10.004>, 2019.

<https://doi.org/10.5194/tc-2022-238>

Preprint. Discussion started: 22 December 2022

© Author(s) 2022. CC BY 4.0 License.



885 Zhang, S., Zhao, H., Sheng, Y., Chen, S., Li, G., & Chen, F.: Late Quaternary lake level record of Orog Nuur, southern
886 Mongolia, revealed by optical dating of paleo-shorelines, *Quat. Geochronol.*, 72, 101370,
887 <https://doi.org/10.1016/j.quageo.2022.101370>, 2022.
888



889 **LIST OF TABLES**

- 890 Table 1. LGM ELA reconstruction
891 Table 2. Result of ^{10}Be exposure age dating
892 Table 3. Run and site parameters for the 2D ice surface model
893 Table 4. Input parameters of glacial mass balance model

894

895 **LIST OF FIGURES**

- 896 Figure 1. Study area
897 Figure 2. The present-day climate of Mongolia
898 Figure 3. Photo composites of the Ih Artsan valley and paleoglacial evidence
899 Figure 4. Geomorphologic setting and moraine stratigraphy in Jargalant valley
900 Figure 5. ^{10}Be Exposure ages (ka) for moraine sequences
901 Figure 6. Kernel Density Plot (KDP) of estimated ^{10}Be exposure ages from distal moraine crests in Jargalant and Ih
902 Artsan valleys
903 Figure 7. Asynchronous distribution in potential clear-sky direct solar radiation, glacial melt, and vegetation
904 Figure 8. Temporal and spatial distributions of glacial and paleo-lacustrine records in the neighboring regions of Ih
905 Bogd massif
906 Figure 9. Asynchronous advance and retreat pattern of Ih Bogd paleo glacier during 22-16 ka
907 Figure 10. Rockfall deposits in Jargalant valley
908 Figure 11. Inheritance from the uplifted paleo-surface of Ih Bogd



909 **Table 1.** LGM ELA reconstruction

Sites	Top of the rock cliff (m a.s.l)	Altitude of cirque floor (m a.s.l)	Headwall altitude ^a (m a.s.l)	Toe altitude, LGM ^b (m a.s.l)	THAR ELA ^c (m a.s.l)
Jargalant valley	3620	3360	3533	2997	3308
Ih Artsan valley	3560	3385	3508	3222	3388
Average					3348

910 ^a Headwall altitude for LGM glaciers was selected at one-third of the altitude difference between the top of the rock
911 cliff and the cirque floor (Goldthwait, 1970).

912 ^b Toe altitude was selected as the minimum altitude of the terminal moraine

913 ^c THAR of 0.58 was used for calculating LGM ELA (Batbaatar et al., 2018)

914



Table 2. Result of ^{10}Be exposure age dating

Moraine group	Name	Latitude (°N, DD)	Longitude (°E, DD)	Elevation (m a.s.l.)	Thickness (cm)	Shielding factor ^a	Quartz ^c (g)	Be carrier ^d (g)	$^{10}\text{Be}/\text{Be}^{e,f}$ (10^{-13})	^{10}Be conc. ^{d,f} (10^5 atoms g^{-1})	Exposure age ^{f, g, h} (ka)	
											St	LSDn
M_{11}	IAM001	44.95421	100.2602	3289	2	0.7746	20.3	0.3729	6.0 ± 0.2	7.7 ± 0.3	22.1 ± 1.9	19.9 ± 1.4
	IAM002	44.95429	100.26022	3290	2.5	0.7746	17.52	0.3796	5.3 ± 0.2	8.0 ± 0.3	23.1 ± 2.0	20.7 ± 1.4
	IAM003	44.95427	100.2603	3289	3.5	0.7746	20	0.3849	6.1 ± 0.2	8.1 ± 0.3	23.7 ± 2.1	21.2 ± 1.5
	IAM004	44.95438	100.26035	3289	3.5	0.7746	14.69	0.3958	4.1 ± 0.1	7.6 ± 0.3	22.1 ± 1.9	19.9 ± 1.4
	IAM005	44.95435	100.26015	3290	3	0.7746	19.75	0.3704	5.7 ± 0.2	7.4 ± 0.2	21.4 ± 1.8	19.3 ± 1.3
	IAM006	44.95437	100.26006	3288	3.5	0.7746	19.54	0.3812	5.7 ± 0.2	7.7 ± 0.2	22.6 ± 1.9	20.3 ± 1.4
	IAM007	44.95438	100.26004	3288	4	0.7746	18.96	0.3738	5.3 ± 0.2	7.2 ± 0.2	21.2 ± 1.8	19.1 ± 1.3
M_{14}	JAM001	44.97614	100.29007	3412	3	0.8218	16.91	0.3842	78.6 ± 0.6	124.9 ± 1.6	344.6 ± 30.1	278.9 ± 18.1
	JAM002	44.97627	100.29012	3411	4	0.8218	20	0.3993	57.0 ± 0.6	79.7 ± 1.1	214.7 ± 18.2	177.3 ± 11.3
	JAM003	44.97651	100.29021	3411	2.5	0.8218	20.03	0.3871	194.3 ± 1.2	262.9 ± 3.1	806.4 ± 79.3	636.2 ± 45.1
	JAM004	44.97654	100.28988	3409	3	0.8218	20	0.382	70.9 ± 0.6	94.8 ± 1.3	256.3 ± 21.9	208.9 ± 13.3
	JAM005	44.97665	100.29008	3409	2.5	0.8218	20.03	0.375	64.8 ± 0.5	84.9 ± 1.1	227.0 ± 19.2	186.6 ± 11.8
M_{13}	JAM006	44.97891	100.29092	3350	3	0.8363	20.02	0.3708	12.3 ± 2.6	15.9 ± 3.4	41.5 ± 9.5	35.9 ± 8.0
	JAM007	44.97886	100.29079	3351	3	0.8363	20.03	0.3707	25.3 ± 5.0	32.8 ± 6.5	86.3 ± 18.9	74.1 ± 15.7
	JAM008	44.97894	100.29084	3350	3	0.8363	20.42	0.3932	68.9 ± 7.0	92.9 ± 9.5	255.2 ± 35.3	209.0 ± 26.1
	JAM009	44.97891	100.29095	3348	3.5	0.8363	19.97	0.3832	15.3 ± 2.7	20.5 ± 3.7	53.8 ± 10.7	45.8 ± 8.7
	JAM010	44.97897	100.29089	3348	3.5	0.8363	19.97	0.3856	40.9 ± 5.7	55.2 ± 7.7	148.7 ± 24.8	123.8 ± 19.4
M_{12}	JAM011	44.98058	100.29328	3293	2.5	0.8598	19.91	0.3903	52.3 ± 0.5	71.7 ± 1.0	194.5 ± 16.4	162.1 ± 10.2
	JAM012	44.98083	100.29321	3289	2	0.8598	19.97	0.3785	93.6 ± 0.6	124.2 ± 1.5	349.1 ± 30.5	284.9 ± 18.4
	JAM013	44.98095	100.29263	3289	4	0.8598	20.22	0.3794	81.0 ± 4.1	106.4 ± 5.5	300.5 ± 30.6	246.6 ± 20.6
	JAM014	44.98096	100.29259	3292	3	0.8598	20.38	0.3812	61.0 ± 6.4	79.9 ± 8.4	218.9 ± 30.5	181.9 ± 23.0
	JAM015	44.98096	100.2926	3292	3	0.8598	20.04	0.3894	59.4 ± 5.2	80.8 ± 7.1	221.7 ± 27.6	184.0 ± 20.3
M_{11}	JAM016	44.98224	100.29684	3193	3.5	0.8852	19.91	0.3872	3.0 ± 0.1	4.0 ± 0.2	10.8 ± 1.0	10.6 ± 0.8
	JAM017	44.98232	100.29693	3191	3	0.8852	20.05	0.3935	4.8 ± 0.3	6.6 ± 0.4	17.7 ± 1.7	16.3 ± 1.4
	JAM018	44.98232	100.29693	3191	2.5	0.8852	20.06	0.3864	5.8 ± 0.4	7.8 ± 0.5	20.8 ± 2.1	18.9 ± 1.7
	JAM019	44.98326	100.29745	3170	3	0.8935	20.17	0.3962	4.4 ± 0.2	6.0 ± 0.3	16.2 ± 1.6	15.1 ± 1.3
	JAM020	44.98379	100.29716	3172	3.5	0.9311	20.14	0.3865	5.8 ± 0.2	7.7 ± 0.2	19.9 ± 1.7	18.2 ± 1.2
Summit Plateau ^j	JAM021	44.98385	100.29712	3171	3	0.9311	20.04	0.3879	5.4 ± 0.2	7.3 ± 0.2	18.9 ± 1.6	17.4 ± 1.2
	SP001	44.58333	100.1725	3625	2.5	1	20.03	0.3871	194.3 ± 1.2	262.9 ± 3.1	560.8 ± 51.7	442.3 ± 29.8
	SP002	44.58333	100.1725	3625	3	1	20.02	0.3708	12.3 ± 2.6	15.9 ± 3.4	27.1 ± 6.2	23.4 ± 5.2



^a Sampling thickness of the boulders' outermost exposed surfaces.

^b Topographic shielding factors for each sampling site were measured at intervals of 30°.

^c Weight of the pure quartz. The density of granite (2.7 g cm^{-3}) was used to calculate exposure age.

^d A mean value of process blank samples ($4.53 \times 10^{-15} \pm 1.62 \times 10^{-15}$) was used for correction.

^e Ratios of $^{10}\text{Be}/^9\text{Be}$ were normalized with 07KNSTD reference sample 5-1 prepared by Nishiizumi et al. (2007) with a $^{10}\text{Be}/^9\text{Be}$ ratio of $2.71 \times 10^{-11} \pm 4.71 \times 10^{-13}$ (calibrated error) and using a ^{10}Be half-life of 1.36×10^6 years (Chmeleff et al., 2010; Korschinek et al., 2010)

^f Uncertainties were calculated at the 1σ confidence level.

^g Exposure ages, assuming zero erosion were calculated using CRONUS-Earth online calculator version 3.0.2 (Balco et al., 2008).

^h Constant production rate of the ^{10}Be model of Stone (2000) was used for calculating exposure age.

ⁱ Constant production rate of the ^{10}Be model of Lifton et al. (2014) was used.

^j SP001 and SP002 (SP is abbreviation of summit plateau) are not real samples. Exposure ages for summit plateau were calculated using the highest and lowest ^{10}Be concentration of boulders from inner moraines from Jargalant and production rate of summit plateau (3625 m a.s.l)



2 **Table 3.** Run and site parameters for the 2D ice surface model

Variable	Value	Unit
Time interval	22-16	ka
Day type	1 (calendar day)	
Day interval	152-243 (summer)	
Average elevation of site	3265.3	m
Modern summer temperature of Ih Artsan	5.4	°C
Modern summer temperature of Jargalant	4.9	°C
LGM anomaly	-5.5	°C
Snow ratio when temperature is below 0°C	0.35	
Elevation of initial glacier's toe (Ih Artsan)	3385.1	m
Elevation of initial glacier's toe (Jargalant)	3360.9	m
Elevation of the distal moraine (Ih Artsan)	3222.2	m
Elevation of the distal moraine (Jargalant)	2997.2	m
Headwall altitude (Ih Artsan)	3508.3	m
Headwall altitude (Jargalant)	3533.3	m
Glacial bed shear stress (Ih Artsan)	100	kPa
Glacial bed shear stress (Jargalant)	200	kPa

3

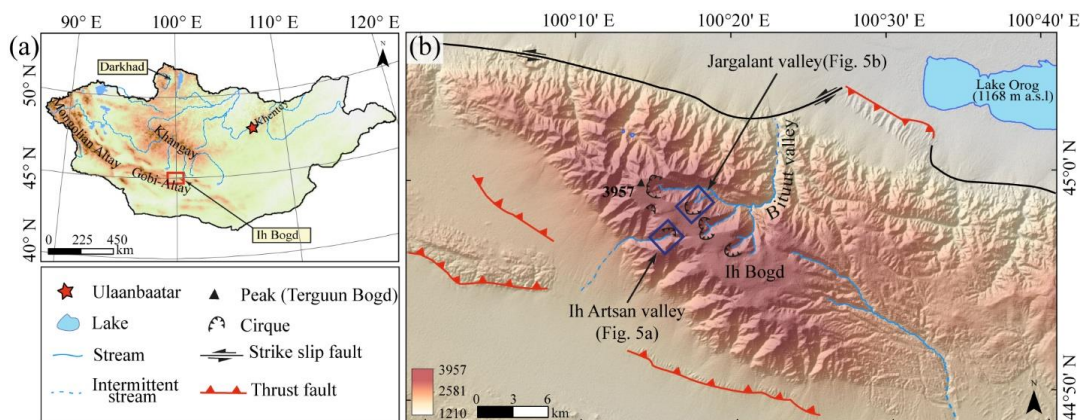
4



5 **Table 4.** Input parameters of glacial mass balance model

Variable	Optimized values/Unit	Variable	Optimized values/Unit
Mass balance calculation (m, mm)		Air pressure calculation (P_h, Pa)	
c	Accumulation mm	P_0	Pressure at reference point (sea level) 1013.25 Pa
a	Ablation/melt mm	T_h	Air temperature at the height h Pa
Melt calculation (a, mm)		T_0	Air temperature at the reference point 288.15 K
n	Number of time steps per day	M	Mass per air molecule 0.0290 kg mol ⁻¹
MF	Melt factor 1.8 mm d ⁻¹ °C ⁻¹	g	Acceleration due to gravity 9.8067 m s ⁻²
a_{ice}	Radiation coefficient for ice surfaces 0.0008	R	Universal gas constant 8.3143 mol K
I	Potential clear-sky direct solar radiation at the glacier W m ⁻²	L	Atmospheric lapse rate -0.008 K m ⁻¹
T	Monthly air temperature °C	Zenith angle calculation (Z, °) and angle of incidence (θ, °)	
Insolation calculation (I, w m⁻²)		δ	Solar declination angle °/Radian
I_0	Solar constant 1367 W m ⁻²	φ	Latitude °/Radian
R_m/R	Eccentricity correction factor of the earth's orbit	ω	Hour angle °/Radian
Ψ_a	Atmospheric transmissivity 0.75	β	Slope inclination angle °/Radian
P_h	Air pressure at the height Pa	γ	Surface azimuth angle °/Radian
P_0	Air pressure at reference point (sea level) 1013.25 Pa		
Z	Zenith angle °		
θ	Angle of incidence °		

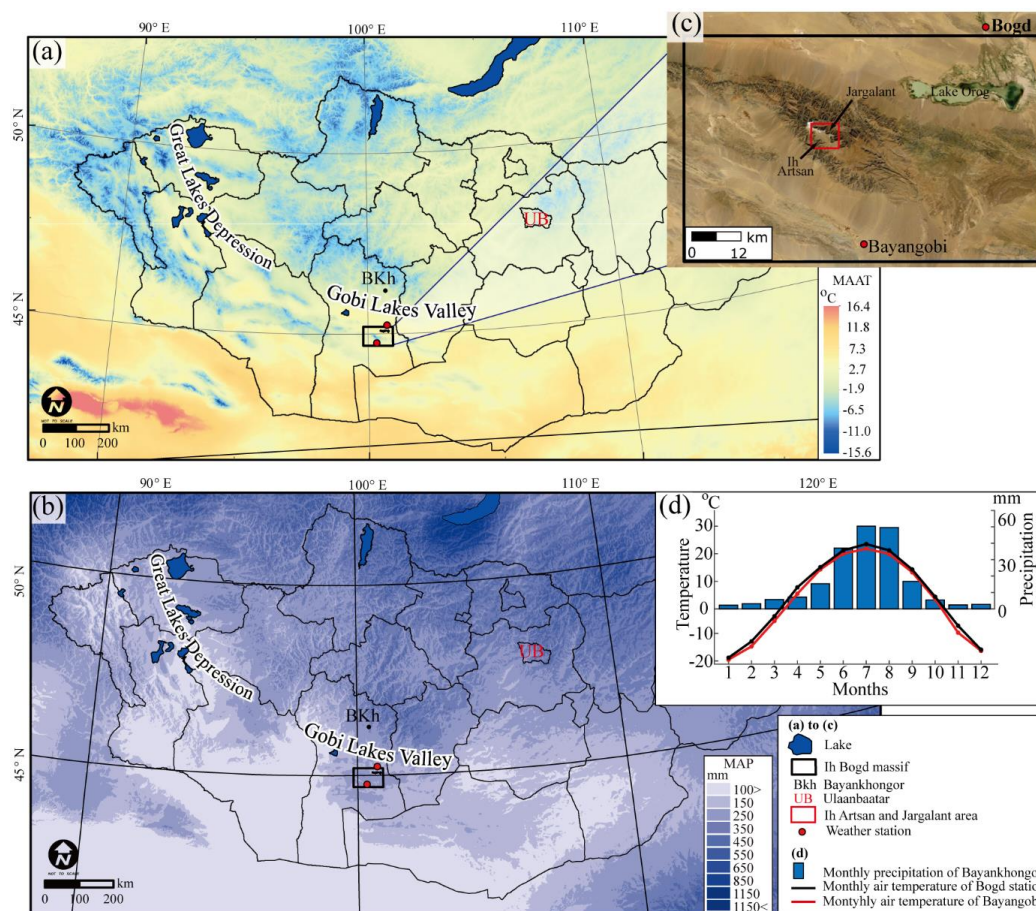
6



7

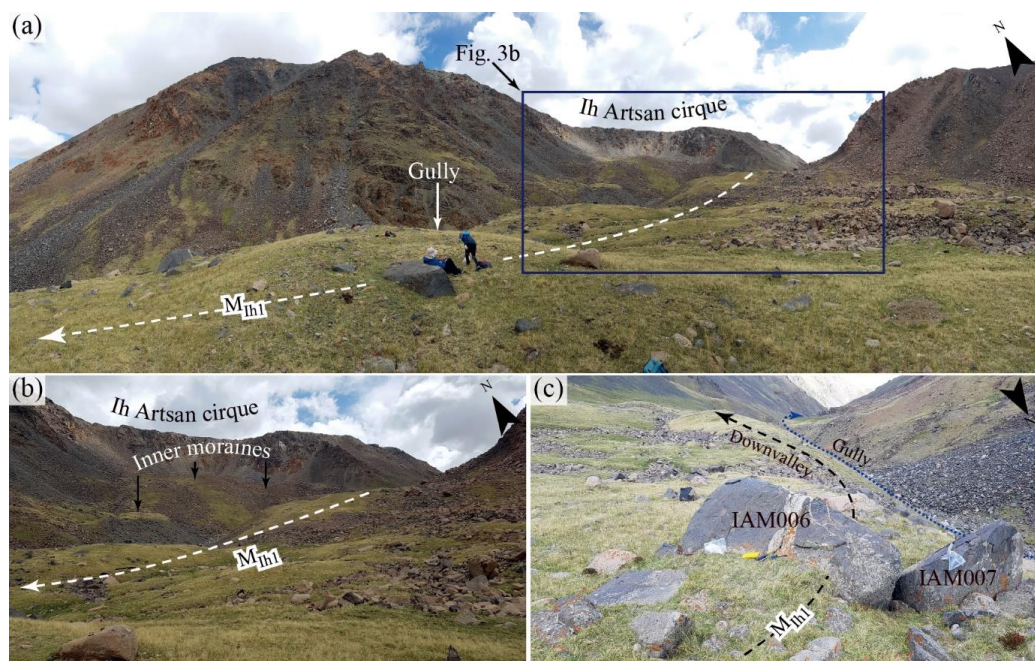
8 **Fig. 1.** Study area. (a) Location of the study area on the map of Mongolia. Ih Bogd massif is described as a red box.
9 (b) Detailed map of the study area. Boxed areas show Ih Artsan and Jargalant valleys which were glaciated during late
10 Quaternary. Detailed maps of both valleys were visualized in Fig. 3-5. The background image is shaded SRTM DEM
11 with 30 m resolution.

12



13

14 **Fig. 2.** The present-day climate of Mongolia. (a) Mean annual air temperature across Mongolia. (b) Mongolian mean
 15 annual precipitation. BKh (black dot) represents Bayankhongor aimag center (largest unit of the Mongolian province),
 16 and UB is Ulaanbaatar, the capital of Mongolia. Red dots mark the nearest weather stations to the study area.
 17 Temperature data (CHELSA_Bio10_01, at 30 arc-second) and precipitation data (CHELSA_Bio10_12, at 30 arc-
 18 second) are long-term (1973-2013) annual means. Source: Bioclim Bio1 data, CHELSA V 1.2 (Karger et al., 2017).
 19 (c) The exact locations of the nearest weather stations to the massif, Bayangobi (1540 m a.s.l) and Bogd (1240 m a.s.l).
 20 (d) Long-term (1989-2019) monthly mean temperature from Bogd station (black line) and Bayangobi station (red line).
 21 Monthly mean precipitation (2005-2019) of Bayankhongor is described as blue bar chart (NAMEM, 2020).



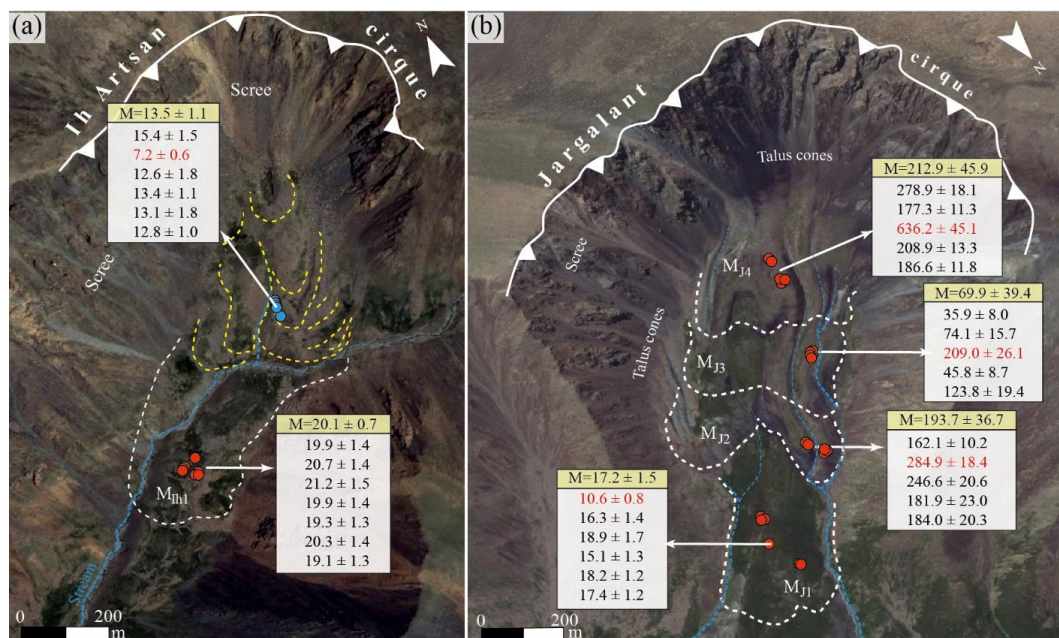
22

23 **Fig. 3.** Photo composites of the Ih Artsan valley and paleoglacial evidence. (a) Ih Artsan glacial cirque and distal
24 moraine ridge. The white dashed arrow represents M_{Ih1} moraine ridge, which marks the farthest extent of late
25 Quaternary glaciation. (b) Distal and inner moraine sequences (Batbaatar et al., 2018). (c) IAM006 and IAM007
26 sampling boulders are on the M_{Ih1} moraine ridge.



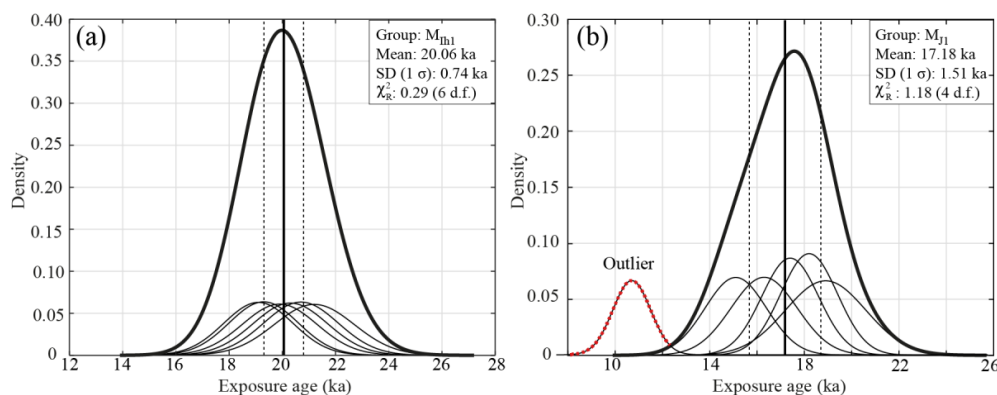
27

28 **Fig. 4.** Geomorphologic setting and moraine stratigraphy in Jargalant valley. (a) Jargalant valley and Bituut trunk
29 valley that rises from the cirque near the highest peak (3957 m a.s.l). Jargalant valley is one of the larger tributary
30 valleys of Bituut valley, while covered by a large amount of last Quaternary moraine complex. (b) The stratigraphic
31 boundary between M_{J4} and M_{J3} moraines in the Jargalant cirque. Moraines are dissected by longitudinal gullies. (c)
32 Pair of M_{J2} moraine and oldest M_{J1} moraine ridge. Horses (red circle) are for scale. (d) Boulder sizes on M_{J2} moraine
33 range from sub-meter to several meters. (e) Downvalley view of the moraine sequences from the uppermost moraine
34 sequence.

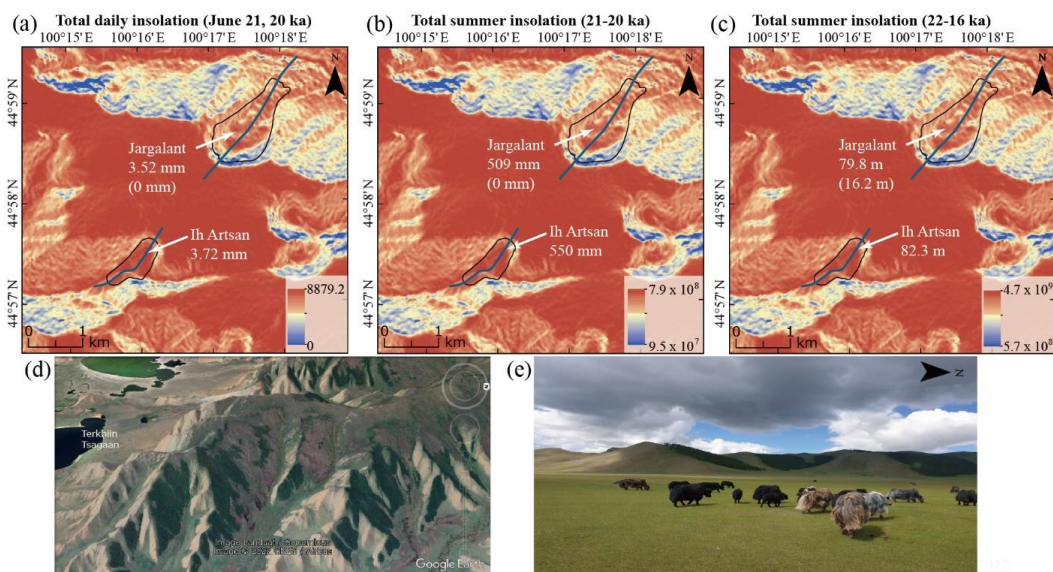


35

36 **Fig. 5.** ^{10}Be Exposure ages (ka) for moraine sequences. (a) Ih Artsan glacial cirque. Individual moraine sequences are
 37 marked by dashed white lines. Moraine ridges in yellow dashed lines indicate inner moraine sequences recognized in
 38 the previous study by Batbaatar et al. (2018). Blue dashed lines show intermittent stream channels. Red circles are the
 39 locations of boulder samples in this study, whereas blue circles indicate the sampling location from Batbaatar et al.
 40 (2018). (b) Jargalant cirque moraine complex, $M_{J4} \sim M_{J1}$. Exposure ages in red are outliers out of one sigma. Outlier
 41 excluded mean age (M) of each moraine sequence is written on the top (yellow background).



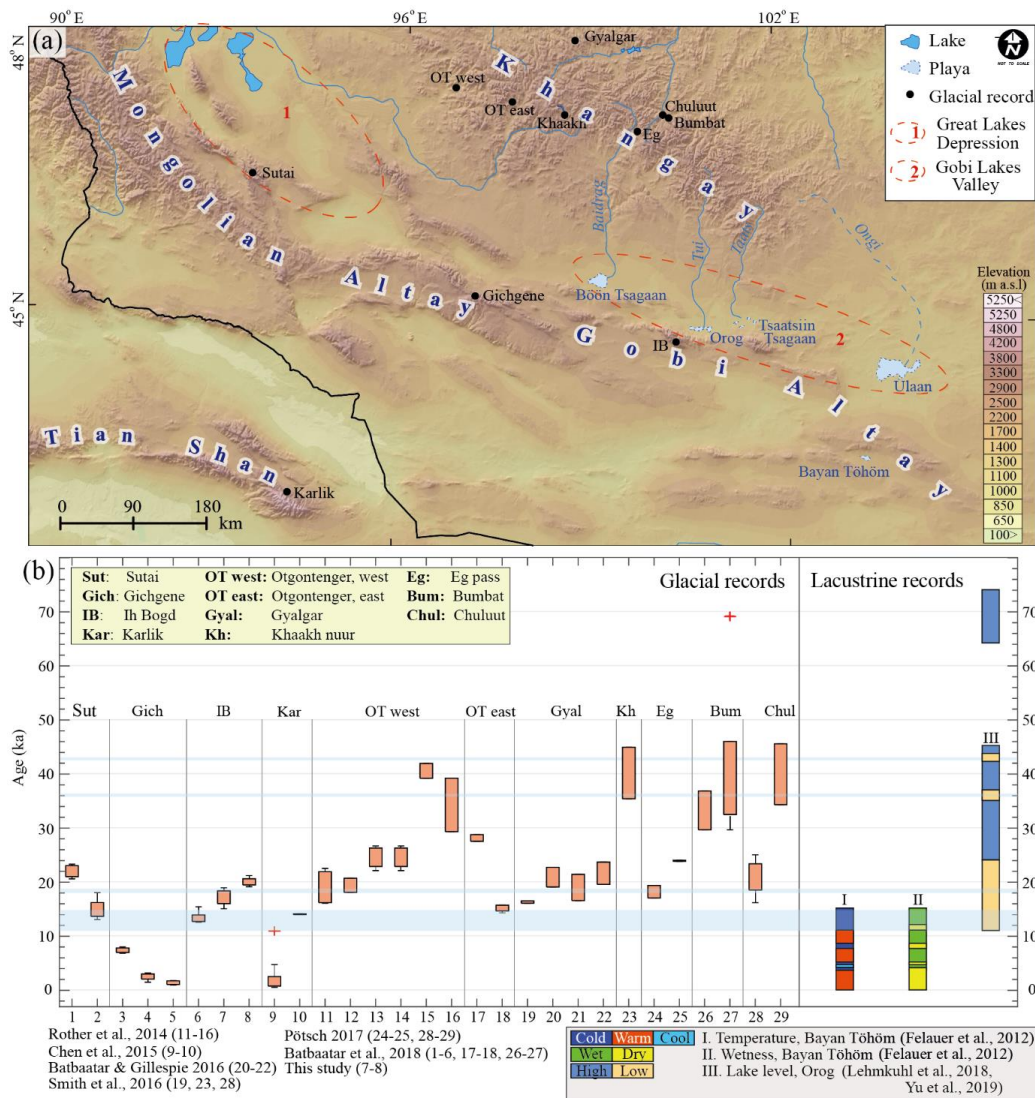
42
43 **Fig. 6.** Kernel density plot (KDP) of estimated ^{10}Be exposure ages from distal moraine crests in Jargalant and Ih Artsan
44 valley. Plots were created using IceTEA Matlab code by Jones et al. (2019). (a) KDP of exposure ages of the most
45 extensive moraine sequence (M_{Ih1}) in Ih Artsan valley. No outlier was detected. The arithmetic mean was calculated
46 and marked as a bold solid vertical line. (b) KDP of exposure ages from the oldest (M_{J1}) moraine sequence in Jargalant
47 valley. The outlier was excluded by Chauvenet, Pierce, and the standardized deviation method in the 1 sigma range.
48 The thick solid lines represent the cumulative density curve, the dashed red line shows excluded outlier, and solid,
49 narrow black lines show individual density curves for each sample. 1 sigma range of the group is marked as two
50 vertical dashed lines. The sample statistics were calculated after rejecting outliers, while external errors were used to
51 create KDP and calculate sample statistics.



52

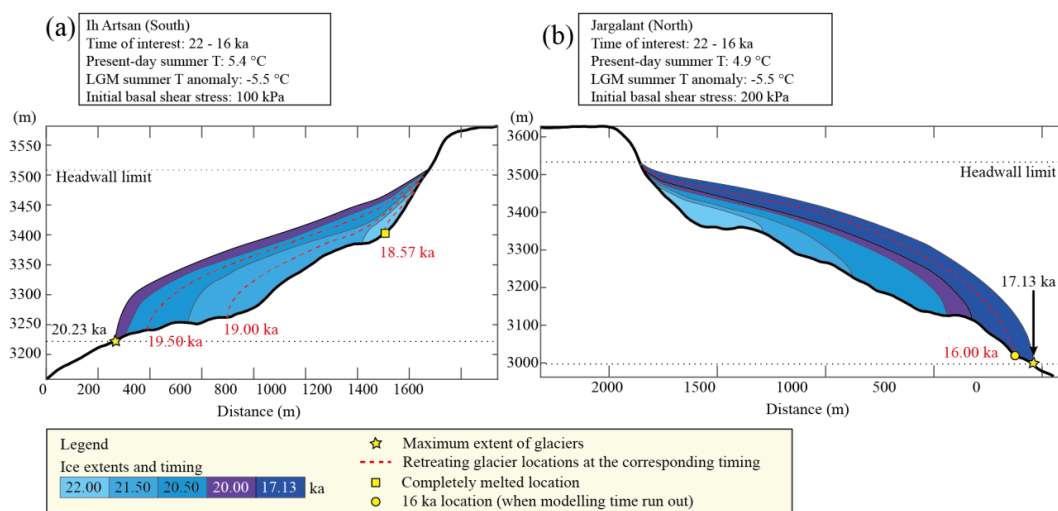
53 **Fig. 7.** Asynchronous distribution in potential clear-sky direct solar radiation (WH m^{-2}), glacial melt, and vegetation.
54 (a) Daily insolation in the summer solstice, 20 ka. (b) Total clear-sky direct solar radiation during 21-20 ka. (c) Total
55 summer insolation for 22-16 ka. Raster map shows integrated total daily insolation and summer insolation. The blue
56 line represents profile along midline in Ih Artsan and Jargalant valley. Average melt along this profile is written in
57 white text in mm and m (See supplementary file 2). Melt when the present-day temperature in Jargalant is considered
58 $0.5\text{ }^{\circ}\text{C}$ (LGM anomaly is the same, $-5.5\text{ }^{\circ}\text{C}$) colder than Ih Artsan is written in parenthesis. (d, e) Tree distribution
59 pattern in northern and southern slope. Both of © Google Earth (2022) imagery (d) and photo (e) present mountain to
60 the north of lake Terkhiin Tsagaan, Khangay mountains.

61



62

63 **Fig. 8.** Temporal and spatial distributions of glacial and paleo-lacustrine records in the neighboring regions of Ih Bogd
 64 massif. (a) Locations of the ^{10}Be age dating sites for paleo-glaciers and paleo lacustrine proxies. (b) Age dating results
 65 from glaciers and lacustrine proxies. Glacial records on the left are the ^{10}Be exposure age dating results representing
 66 29 individual moraine groups. Exposure ages were recalculated with Cronus Earth V3, using the LSDn scaling factor
 67 (Lifton et al., 2014). Only effective ages were plotted after outlier rejection using the normalized deviation method
 68 (Batbaatar et al., 2018). The shaded light blue sections on the age interval present the major harsh periods (playa phase
 69 of Orog, Yu et al., 2019). Lacustrine records on the right present temperature (I) and wetness data (II) in lake Bayan
 70 Töhöm and lake level record of lake Orog (III).



71

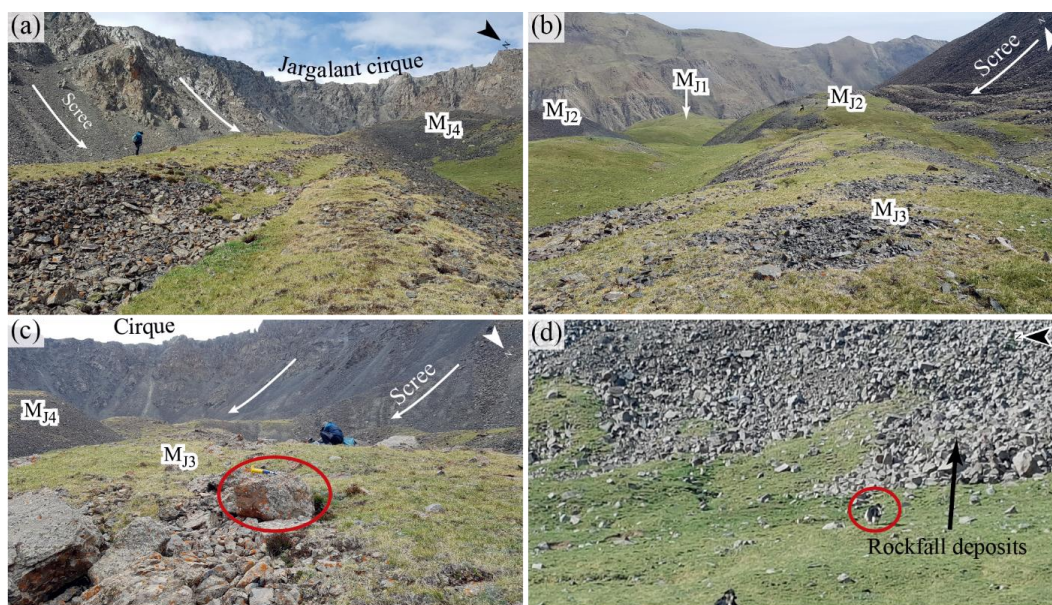
72 **Fig. 9.** Asynchronous advance and retreat pattern of Ih Bogd paleo glacier during 22-16 ka. (a) Paleo-glacier in Ih
73 Artsan valley maximally advanced in 20.23 ka. (b) Paleo-glacier in Jargalant valley most expanded in 17.13 ka. The
74 present-day summer paleotemperature in the north-facing valley was considered 0.5 °C lower than in the south-facing
75 valley. The present-day temperature is calibrated to Greenland (NGRIP) paleotemperature data (Buizert et al., 2018)
76 using an LGM summer temperature anomaly of -5.5 °C. Headwall altitudes of the LGM paleo glaciers were used to
77 mark the maximum thickness of the glacier.

78

79

80

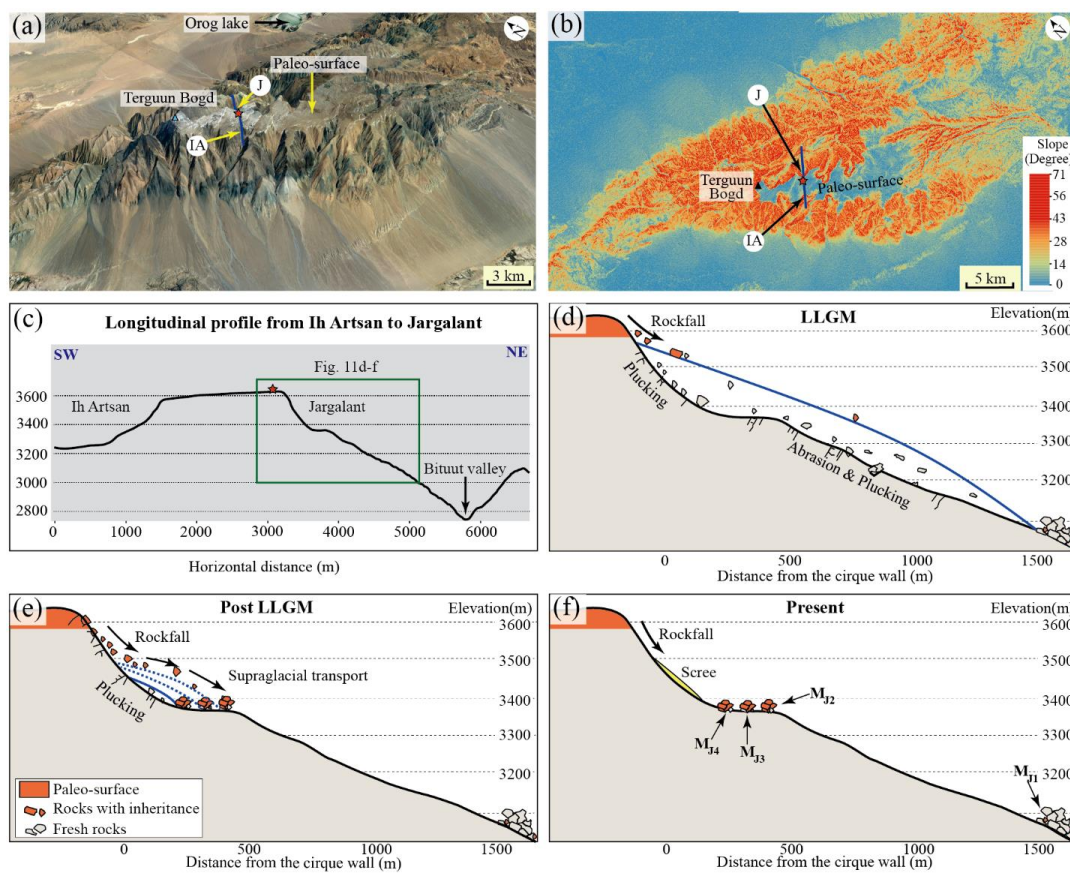
81



82

83 **Fig. 10.** Rockfall deposits in Jargalant valley. The scree or talus cone was on the cirque wall. M_{J4} , M_{J3} , and M_{J2}
84 moraine formed within a Jargalant cirque, consequently outer edges of moraine ridges near the cirque wall were
85 covered with talus deposit. (a) Rockfall deposit on the southeastern cirque wall, near M_{J4} moraine. (b) Scree covering
86 on M_{J2} moraine that is dissected by an intermittent stream. (c) Sampling site of M_{J3} moraine and scree on the southern
87 and southwestern wall of the cirque, near M_{J4} , M_{J3} moraine. JAM010 was taken from the circled boulder. Chisel, for
88 scale, is on the boulder. (d) Rockfall deposit on the eastern slope of the cirque. Yak (circled) for scale.

89



90

91 **Fig. 11.** Inheritance from the uplifted paleo-surface of Ih Bogd massif. (a) 3D view of the paleo-planation surface (©
 92 Google Earth, 2022). (b) Slope map of Ih Bogd, location of the Ih Artsan (IA) and Jargalant (J) valley. The green
 93 triangle represents the highest peak of the massif, Terguun Bogd. Exposure age and erosion rate (Table 2) were
 94 calculated using the highest concentration of the boulder from M_{J4} - M_{J2} (Fig. 11a) for the point location marked as red
 95 star (Fig. 11b; 3625 m). (c) Longitudinal profile along a dark blue line (See Fig. 11b) connecting Ih Artsan and
 96 Jargalant valley from SW to NE. (d) LGM glacial extent and intensive plucking of fresh rocks. (e) A series of M_{J4} ,
 97 M_{J3} , and M_{J2} moraines formed by successive glacial advances. According to a shortage of glacier length and thinning
 98 of ice surface near cirque, less bed plucking, and more rockfall events from the paleo surface may have occurred. (f)
 99 Present-day rockfall deposit without supraglacial transport.

100